LITHOS 488-489 (2024) 107828

Contents lists available at ScienceDirect

LITHOS

journal homepage: www.elsevier.com/locate/lithos

Supergene formation of sulfur-rich, tochilinite-bearing serpentinites in the Oman ophiolite

James Andrew Leong [a,b,*], Juan Carlos de Obeso [c], Thomas Sharp [d], Everett Shock [d], Peter Kelemen [a]

[a] Lamont-Doherty Earth Observatory, Columbia University, NY, USA
[b] Department of Geology and Environmental Earth Science, Miami University, OH, USA
[c] Department of Geology and Geophysics, University of Utah, UT, USA
[d] School of Earth and Space Exploration, Arizona State University, AZ, USA

ARTICLE INFO

Keywords:
Serpentinization
Sulfide
Supergene enrichment
Tochilinite
Nickel
Thermodynamic model

ABSTRACT

Mass transfer processes between fluids and ultramafic rocks produce subsurface environments encompassing a wide range of redox conditions. A notable locality where an extensive range of redox conditions is observed in one location is Hole BA1B, a ~ 400 m borehole drilled by the Oman Drilling Project. A sulfur-enriched serpentinite zone, containing up to 0.6 wt% S, occurs between shallow oxidized serpentinites (<30 m) and deep partially serpentinized harzburgite (>150 m). All three alteration zones are predominantly composed of serpentine. However, microanalysis of samples from the sulfur-enriched zone shows that mesh textures after olivine are composed of serpentine, brucite, and tochilinite mixtures, yielding optically black thin-section samples that characterize this sulfidic zone. It is proposed that sulfur accumulates in this zone via a process similar to those found in supergene ore deposits. Reaction-path models show that at shallow conditions open to atmospheric input, sulfur is mobilized via oxidative weathering of serpentinized dunite and harzburgite. Sulfate-bearing fluids percolate deeper and react with host rocks in a system closed to atmospheric input. As fluids become more reduced, dissolved sulfate is precipitated as sulfide minerals yielding rocks with ~0.4 wt% S, like those observed in Hole BA1B. Despite enrichment of S in the sulfidic zone in Hole BA1B, Ni and Co contents are uniform throughout all three layers in the borehole. This is consistent with model results which show that Ni (and, by analogy, Co) is less mobile than S, and can be hosted in serpentine and NiFe alloys in addition to sulfides. The sulfur enrichment process may occur abiotically. However, sulfide enrichment via microbial reduction of sulfate and other sulfur species can also facilitate the formation of the sulfidic zone. Bioenergetic calculations show that abundant energy is available for sulfur reducing microbes, consistent with previous work demonstrating the presence of active, sulfate-reducing microorganisms in Hole BA1B and other nearby boreholes. This suggests that the observed sulfur enrichment is an ongoing process. Overall, this work shows that variable redox conditions are attained as fluids percolate and react with serpentinized ultramafic rocks at variable extents of interaction between aquifer fluids, host ultramafic rocks, and the atmosphere.

1. Introduction

Ultramafic rocks from the Earth's mantle are unstable when emplaced at the Earth's surface. At or near the Earth's surface, reactions hydrate, oxidize, and carbonate the minerals that comprise ultramafic rocks. This process, known as serpentinization, produces serpentinite rocks which are mostly composed of minerals from the serpentine group with or without brucite, iron oxides, carbonates, and other accessory minerals. Serpentinites can be further altered when local conditions change, forming several generations of serpentine veins and textures. This process is not limited to magmatically-driven hydrothermal environments, where rocks are altered by circulating hot fluids. Serpentinization can occur ubiquitously whenever and wherever water meets ultramafic rocks, and over a wide range of temperature, aqueous, and redox conditions. Oxidized, rust-red colored, serpentine soils are common topsoils of ultramafic masses emplaced in continents, some hosting

* Corresponding author at: Miami University, OH, USA.
E-mail address: leongj@miamioh.edu (J.A. Leong).

https://doi.org/10.1016/j.lithos.2024.107828
Received 30 April 2024; Received in revised form 14 September 2024; Accepted 29 September 2024
Available online 3 October 2024

nickeliferous laterite deposits (Butt and Cluzel, 2013; Golightly, 1981). In contrast, highly reduced (H_2- and CH_4-rich), hyperalkaline (pH >11) springs seeping out from ultramafic rocks are the products of ongoing, low-temperature serpentinization reactions in ultramafic aquifers (Barnes and O'Neil, 1969; Kelemen et al., 2021; Leong et al., 2021; Neal and Stanger, 1985; Paukert et al., 2012). These highly reducing conditions are corroborated by the presence of FeNi-alloys in serpentinized ultramafic rocks (Beard and Hopkinson, 2000; Evans et al., 2023; Frost, 1985; Frost and Beard, 2007). Different generations of serpentine minerals with variable Fe(III)/ΣFe content are commonly observed in one hand sample (Ellison et al., 2021; Mayhew and Ellison, 2020). Sulfides of variable oxidation states are known to occur in serpentinites (de Obeso and Kelemen, 2020; Kelemen et al., 2021; Klein and Bach, 2009; Schwarzenbach et al., 2012, 2014). All these observations indicate that serpentinization can occur over a variety of redox conditions. Some redox conditions favor the formation of organic molecules and reduced volatiles that can enable habitable environments deep in the subsurface (Lang et al., 2010; Schrenk et al., 2013; Shock and Canovas, 2010; Templeton et al., 2021). Highly reducing environments attained via serpentinization produce natural H_2 that may be utilized as a clean energy source (Ely et al., 2023; Templeton et al., 2024). Thus, constraining these redox conditions provides insights into the habitable zones and economic resources found in ultramafic-hosted environments. Aside from Earth, ultramafic rocks are widespread in the solar system, and water present in contact with these rocks yields redox environments that may enable life outside our own planet (Glein and Zolotov, 2020).

A notable example that demonstrates this extensive range of redox conditions observed in one location is Hole BA1B (Kelemen et al., 2021), a ~ 400 m borehole drilled by the Oman Drilling Project (OmanDP), an International Continental Drilling Program (ICDP) endeavor participated in by >200 scientists who comprise the OmanDP team (Kelemen et al., 2020a). A sulfur-enriched serpentinite zone (up to 0.6 wt% S) occurs between shallow, reddish, oxidized serpentinites (<30 m) and deeper, dark-green, partially serpentinized harzburgite (>150 m). The sulfidic zone is characterized by optically black thin-section samples (Fig. 11 in Kelemen et al., 2021). It is believed that sulfur enrichment is an ongoing process, consistent with the detection of sulfate-reducing microorganisms in Hole BA1B and nearby boreholes, producing sulfides that can overprint existing serpentinites (Glombitza et al., 2021; Templeton et al., 2021). Quantifying the redox conditions (fH_2S, fH_2, fO_2, f denotes fugacity) in these different zones can reveal geochemical constraints on what makes these environments habitable in this borehole, and in similar low-temperature environments on Earth and beyond. In this work, we quantified these redox conditions through thermodynamic reaction-path simulations. To ground truth model results, outcomes of simulations are compared to analytical observations conducted in this work and previously by others.

2. Hole BA1B and other related boreholes drilled by the Oman Drilling Project

Hole BA1B is one of the seven boreholes that comprise the multi-borehole observatory (MBO) of the Oman Drilling Project (OmanDP). These boreholes were drilled to study ongoing alteration (hydration, oxidation, carbonation) of exposed ultramafic rocks, and its consequences on the subsurface hydrological, geomechanical, and geochemical conditions, and the microbial habitats it can support. The locations of these boreholes, shown in a geological map (Fig. S1, modified from Nicolas et al., 2000), are in the Wadi (valley) Tayin massif of the Samail ophiolite in the Sultanate of Oman. The MBO boreholes are all located in the peridotite section of the ophiolite, and are near the town of Batin, northeast of the city of Ibra in the Al Sharqiyah region of the Sultanate of Oman. All boreholes are located in Wadi Laywani except for Hole BA2A which is in Wadi Mehlah. All seven boreholes (Holes BA1A, BA1B, BA1C, BA1D, BA2A, BA3A, BA4A) were drilled in 2017 and 2018. Three of these boreholes (Holes BA1B, BA3A, BA4A) were drilled via diamond wireline coring with ~100 % recovery. Recovered cores were shipped to Japan and loaded onto the D/V Chikyu where they were described and analyzed by the OmanDP team following protocols similar to those of the International Ocean Discovery Program (IODP). Descriptions of the recovered core are detailed in Kelemen et al. (2020b, BA1 sites), Kelemen et al. (2020c, BA2A), Kelemen et al. (2020d, BA3A), and Kelemen et al. (2020e, BA4A) and summarized in Kelemen et al. (2021). The hydrogeology and hydrogeochemistry of these boreholes are reported in Lods et al. (2020), Nothaft et al. (2021a), and Sohn and Matter (2023). Detailed petrological, petrophysical, isotopic, and mineralogical observations of alteration assemblages in the boreholes are previously reported (de Obeso et al., 2020; Ellison et al., 2021; Hatakeyama et al., 2021; Hong et al., 2022; Katayama et al., 2020; Lima-Zaloumis et al., 2022; Malvoisin et al., 2020; Scicchitano et al., 2021; Templeton et al., 2021; Ternieten et al., 2021). An overview of the microbial and biogeochemical processes observed in these boreholes is given in Templeton et al. (2021).

The primary lithological sequences observed in these boreholes are shown in Fig. 1. Cores from Hole BA1B were recovered up to ~400 m below ground, which is ~100 m deeper than those recovered from Holes BA3A and BA4A. Recovered rocks from these boreholes are mostly peridotite (harzburgite and dunite) with minor occurrences of gabbros and pyroxenites. The upper 150 m of Hole BA1B are composed mostly of dunite with minor occurrences of harzburgite and gabbro. The deeper 250 m of recovered cores from Hole BA1B are mostly harzburgite with minor dunite and gabbro. Hole BA3A is mostly composed of harzburgite while Hole BA4A is mostly dunite. All of these are capped with a thin layer (<1 m in Holes BA1B and BA4A, ~6 m in Hole BA3A) of alluvium.

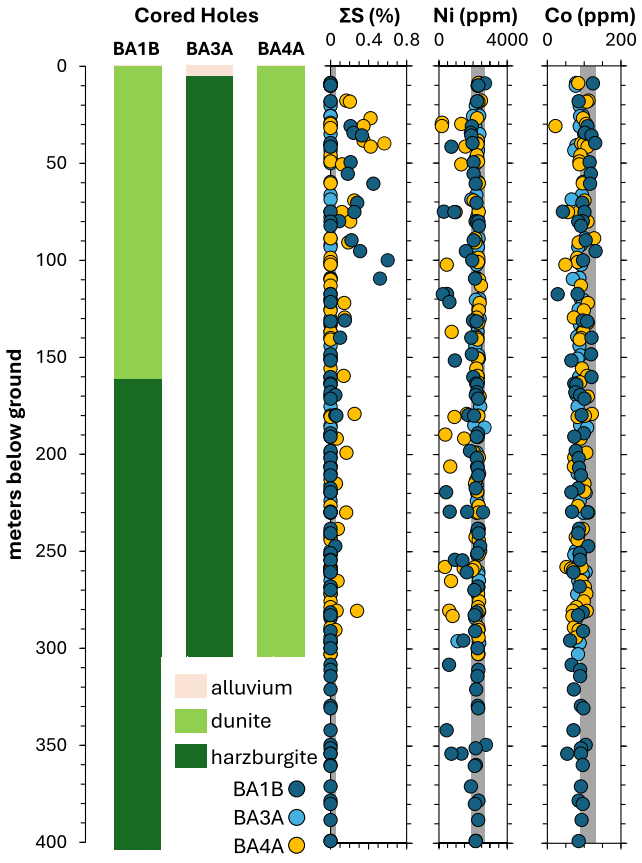

Fig. 1. Downhole primary lithologies identified for Holes BA1B, BA3A, and BA4A, along with the S, Ni, and Co content of discrete downhole samples in these three sites. All data presented in this figure are taken from Kelemen et al. (2020b, 2020d, 2020e). Gray fields indicate concentrations typical of peridotites in the Samail ophiolite (Hanghøj et al., 2010).

A few meters of peridotite core recovered from the near surface parts of the boreholes are highly oxidized, characterized by reddish colored serpentinized peridotites and white carbonate veins (mainly calcite). This transitions into dark green colored serpentinized peridotites characterized by mesh pseudomorph replacement of olivine by serpentine, cross-cut by several generations of serpentine veins. Relict olivine exists throughout the boreholes, especially towards deeper parts, but the overall mineralogy of recovered rocks is dominated by serpentine (Kelemen et al., 2021; Templeton et al., 2021). However, thin section sampling reveals optically black, nearly opaque, serpentinites occurring in Holes BA1B and BA4A that are in contrast with reddish-colored thin sections from rocks recovered from the shallowest cores and transparent to slightly translucent thin sections commonly observed in the deeper partially serpentinized peridotites (Fig. 2, and Figs. 10 and 11 in Kelemen et al., 2021). Optically opaque thin sections are most intense from rocks recovered between 30 and 150 m below the surface in Hole BA1B and are rarely observed at rocks recovered deeper into the borehole (Fig. 2). Nevertheless, optically opaque mesh veins surrounding relict olivine can still be observed from rocks recovered from the deeper parts of Hole BA1B, albeit at lower intensity than those recovered between 30 and 150 m. In Hole BA4A, optically opaque thin sections are commonly observed throughout the 300 m borehole, but are most intense in those recovered from the upper 150 m. In both Holes BA1B and BA4A, these optically opaque sections are from rocks that have the highest total sulfur (ΣS) in the boreholes (Fig. 1), as measured by the shipboard OmanDP team during descriptions aboard the D/V Chikyu (Kelemen et al., 2020b, 2020d, 2020e, and see Fig. 12 in Kelemen et al., 2021). In contrast, in Hole BA3A where optically opaque thin sections are rarely observed, the recovered rocks have ΣS below the detection limit of the shipboard volatile analyzer (see light blue circles in Fig. 1). Measured ΣS from rocks recovered from Holes BA1B and BA4A ranges from below detection to ~0.6 wt%. Optically opaque sections (~0.1 to ~0.6 wt% ΣS) are highly enriched in sulfur relative to representative serpentinized peridotites in the Samail ophiolite (typically <0.05 % or 500 ppm, Hanghøj et al., 2010; Oeser et al., 2012), as well as average seafloor low-temperature serpentinites (0.09 to 0.2 wt% ΣS, Alt et al., 2013), and are on par with maximum sulfur measured from the Atlantis Massif (Delacour et al., 2008). Sulfide-rich dunites near the Moho transition zone were previously recorded in Oman, but are of intrusive igneous origin (Negishi et al., 2013).

In contrast to downhole ΣS trends in Holes BA1B and BA4A, there is no distinct enrichment of other elements typically associated with sulfur (Ni, Co, Cu, Zn, see Fig. 1 for Ni and Co trends) in these sulfur-enriched zones, as measured by the OmanDP team (Kelemen et al., 2020b, 2020d, 2020e). The Ni and Co concentrations trend uniformly downhole and are at levels typical of peridotites in the Samail ophiolite (Godard et al., 2000; Hanghøj et al., 2010; Monnier et al., 2006).

Overall, and particularly in Hole BA1B, visual and thin-section observation by the onsite and shipboard OmanDP team (Kelemen et al., 2020b, 2021) revealed three distinct alteration zones (see Fig. 2): 1) highly oxidized serpentinites (high Fe(III)/ΣFe of up to ~0.9) down to 30 m, 2) sulfidic serpentinites with ΣS up to 0.6 wt% and characterized by optically opaque thin sections between 30 and 150 m, and 3) serpentinized peridotites with the typical transparent to slightly translucent thin sections from 150 m to deeper parts of the borehole. While these three distinct alteration horizons can be visually different, they are mineralogically primarily composed of serpentine (Kelemen et al., 2021; Templeton et al., 2021). The MgO content ranges from 45 to 50 wt%, typical of serpentinites, with a slightly decreasing downhole trend in Hole BA1B indicating increasing pyroxene content of the protolith. Other notable secondary minerals observed in the MBO boreholes are ferrous-iron-rich brucite (Ellison et al., 2021), awaruite (Ni_3Fe, Ellison et al., 2021; Kelemen et al., 2021), andraditic (hydro)garnet ($Ca_3Fe_2(SiO_4)_{3-x}(OH)_{4x}$, Ellison et al., 2021), and tochilinite ($6Fe_{0.9}S\bullet5(Mg,Fe)(OH)_2$, Templeton et al., 2021; Tutolo and Evans, 2018). All of these minerals are redox sensitive, and thus can provide clues to the conditions at which they formed.

The compositions of secondary phases, including sulfide minerals,

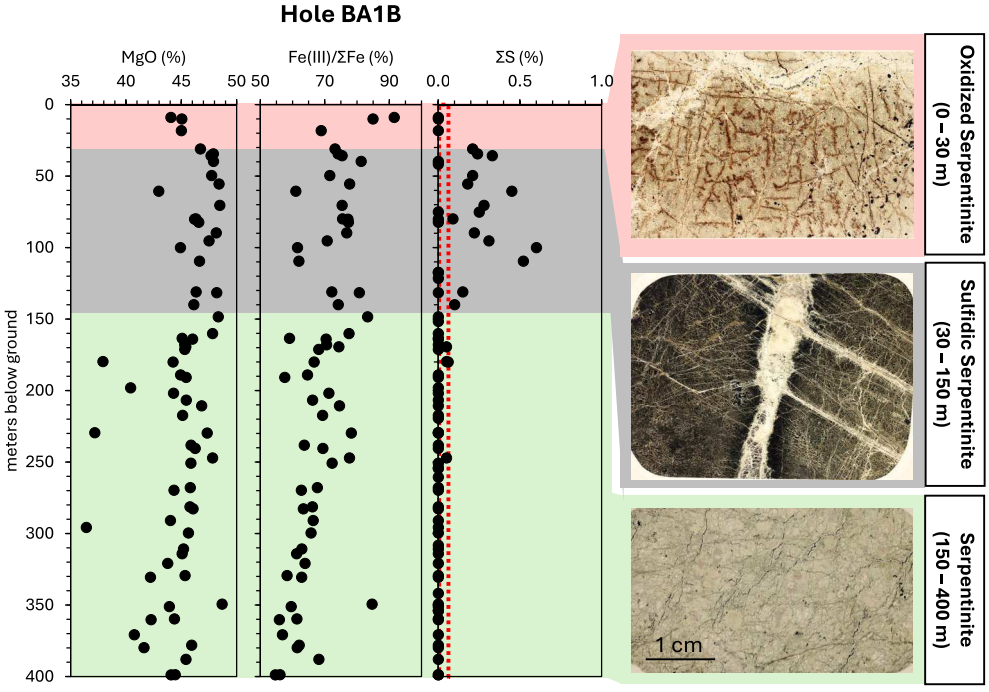

Fig. 2. Downhole data for Hole BA1B. MgO and S content from Kelemen et al. (2020b) while Fe(III)/ΣFe is from Kelemen et al. (2021). The three images on the right are whole thin section scans under transmitted light (from top to bottom: BA1B_05_3_19_22.5 14 m depth, BA1B_44_2_73_78 109 m depth, BA1B_114_4_51_56 321 m depth, in Fig. 10 of Kelemen et al., 2021). Overall, three distinct alteration zones are distinguished for the purpose of this work: oxidized serpentinites, sulfidic serpentinites, and partially serpentinized peridotite. Dotted red field indicates typical S content measured in other Samail ophiolite peridotites (Hanghøj et al., 2010). (For interpretation of the references to colour in this figure legend, the reader is referred to the web version of this article.)

were reported in detail by Ellison et al. (2021), Kelemen et al. (2021), and Templeton et al. (2021). A supergene origin for the sulfidic alteration zone was proposed by Kelemen et al. (2021) informed by a combination of mineralogical analysis and mass-transfer thermodynamic modeling. In this work, we expand previous models by accounting for additional relevant minerals (e.g., Ni solid solutions in serpentine, oxyhydroxides) which were not included previously. New calculations simulate relevant pressure conditions (50 bars) whereas calculations shown in Kelemen et al. used a thermodynamic database commonly for seafloor hydrothermal simulations (500 bars; Klein and Bach, 2009). Both dunite and harzburgite starting materials were modeled in this work while only harzburgite was considered in Kelemen et al. (2021). Micro- to nanoscale analyses of secondary phases were also conducted to comprehensively examine alteration products. We also constrained the redox conditions that lead to the formation of the three alteration zones, as well as mobilization of various elements during the alteration process. In particular, we discuss why we observed enrichment in sulfur but not nickel in the optically opaque zone of Hole BA1B.

3. Materials and methods

3.1. Mineralogical investigation

Recovered rocks from Hole BA1B were described and analyzed onsite and aboard D/V Chikyu. Data can be found in Kelemen et al. (2020b). Detailed descriptions of shipboard methods are given in Kelemen et al. (2020f). Several shipboard thin sections and powders were further analyzed in this work.

Thin sections were analyzed under a Zeiss Axioscope 5 microscope at Columbia University's Lamont Doherty Earth Observatory (LDEO). Petrographic investigations were conducted under plane-polarized, cross-polarized and reflected light. Shipboard thin sections were also analyzed under a JEOL JCM-7000 Neoscope Scanning Electron Microscope (SEM) at LDEO. The SEM is equipped with an energy dispersive spectrometer (EDS) for semiquantitative determination of chemical compositions of analyzed spots (10 μm) and areas in thin sections. Observations were mostly conducted under the backscatter electron mode. Thin sections were also analyzed using the 5-spectrometer Cameca SX5-Tactis electron microprobe analyzer (EPMA) at the American Museum of Natural History (AMNH). The bulk and minor element composition of target spots (10 μm) and areas in thin sections were determined via wavelength dispersive spectroscopy (WDS). Investigations were conducted under 15 keV and 10 nA column conditions. Results of analysis are in Table S1. Lastly, some shipboard-prepared powders were analyzed at LDEO using an Olympus BTX-II Xray Diffractometer (XRD) equipped with a cobalt X-ray tube for mineral identification.

A partially serpentinized peridotite collected from a Samail ophiolite outcrop near the Al Bana hyperalkaline springs (Leong et al., 2021, also see Fig. S1) was also analyzed to examine incipient stages of olivine serpentinization in contrast to those observed at Hole BA1B. A JEOL JXA-8530F EPMA with WDS (15 keV, 10 nA) at Arizona State University (ASU) was used to locate a target for further nanoscale analysis. A transect consisting of olivine altering into a mixture of serpentine and brucite typical of an incipient mesh type replacement was chosen. A Nova 200 Dual Beam Focused Ion Beam (FIB) SEM was used to cut the targeted cross-section for nanoanalysis using the JEOL ARM200F Scanning Transmission Electron Microscope (STEM). The ARM200F is an aberration-corrected STEM equipped with an EDS that enables high spatial resolution imaging and analysis. STEM Imaging modes used were high angle and medium angle annular dark-field as well as brightfield and annular brightfield. Images reported in this work are generated via the brightfield (BF) mode. Imaging and analysis were conducted either with a 120 or 200 kV accelerating voltage. Nanoanalysis and associated sample preparation were conducted at ASU LeRoy Eyring Center for Solid State Science (now Eyring Materials Center).

3.2. Thermodynamic calculations

Mass-transfer reaction-path calculations were conducted to simulate reaction of groundwater with ultramafic rocks. Simulations were divided into two steps, similar to those conducted in previous works (Bruni et al., 2002; Kelemen et al., 2021; Leong et al., 2021; Paukert et al., 2012). The first step simulates reaction of Oman serpentinized peridotites with meteoric-derived groundwater in a system open to atmospheric exchange. Dissolved O_2 and inorganic carbon (ΣCO_2) concentrations are controlled by the O_2 and ΣCO_2 atmospheric partial pressures, respectively. As O_2 and CO_2 are consumed during mineral oxidation and carbonation reactions they are replenished. Simulation starts from the moment the reacting rock begins to dissolve in the fluid until reaching a water:rock ratio of 10 (i.e., 0.1 kg rock reacts with 1 kg of fluid), where accumulated dissolved sodium content is equivalent to shallow groundwaters in Oman (~1 mmolal NaCl, Leong et al., 2021; Nothaft et al., 2021b). In Step 2 of the models, the fluid at the termination of Step 1 is reacted with the same Step 1 reactant rocks but without atmospheric input. That is, when consumed, dissolved O_2 and inorganic carbon are not replenished. Step 2 models simulate percolation of fluids deeper into the aquifers where they can become reduced and hyperalkaline. Step 2 simulations are terminated when the water: rock ratio reaches 0.05 (i.e, 20 kg rock altered by 1 kg of fluid), after most of the starting fluid has been consumed via mineral hydration reactions. Two rocks with compositions representative of an average Oman serpentinized dunite and harzburgite (Hanghøj et al., 2010) were used as the initial compositions (see Table S2). Average global rainwater (Berner and Berner, 2012) was used as the input fluid in Step 1 models. Input fluids for Step 2 models are the ending fluids from Step 1 simulations. Models are for 35 °C and 50 bar to simulate subsurface aquifer conditions in Hole BA1B (50 to 500 m deep).

Reaction-path calculations were conducted through EQ3/6 (Wolery and Jarek, 2003) using a modified thermodynamic database. Thermodynamic data for minerals and aqueous species were mostly the same as those used by Leong and Shock (2020) and Leong et al. (2021). Mineral data were mostly taken from Helgeson et al. (1978) while those for aqueous species were mostly from Shock et al. (1997), Shock and Helgeson (1988) and Sverjensky et al. (1997) together with the revised Helgeson-Kirkham-Flowers equation of state (Shock et al., 1992). Additional data (see Table S3) for Ni-bearing minerals taken from Gamsjäger et al. (2005) and Foustoukos et al. (2015) are also included. The thermodynamic database was compiled via pyCHNOSZ (Boyer, 2021) in the Water-Organic-Rock-Microbe (WORM) portal (https://worm-portal.asu.edu/), which is based on the CHNOSZ thermodynamic calculator (Dick, 2019, https://chnosz.net/).

Disequilibria during mixing of resulting fluids were also quantified to calculate the energy available for microbes that reduce sulfate and other forms of sulfur. Methods for calculating disequilibria are summarized in Shock et al. (2010) and Amend and LaRowe (2019). Energy available from a chemotrophic reaction is given by the chemical affinity (A_r) for the reaction. The chemical affinity is the change in the overall Gibbs free energy (ΔG_r) as the reaction progresses. The A_r in Joules per mole of limiting reactant were calculated and multiplied by the concentrations of the limiting reactant (moles per kg fluid) to derive instantaneous energy available per kg of mixed fluid (Joules per kg fluid). Calculations were conducted with the aid of the aqEquil code in the WORM portal (Boyer et al., 2024).

4. Results

4.1. Mineralogical observations

4.1.1. Oxidized serpentinite (0–30 m below surface)

Samples recovered from the shallowest 30 m of BA1B show large extents of oxidation, exhibited by ubiquitous veins and mesh pseudomorph textures (after olivine) composed of Fe oxyhydroxides. Whole

thin-section scans show abundant red or rust-colored veins as well as red to black colored serpentine mesh textures after olivine (Fig. 3a and b). In contrast to those in mesh textures, serpentine after pyroxene exhibits bastite pseudomorph textures that are mostly free of dark-colored minerals. Late-stage serpentine veins (Fig. 3a, violet label) often have subhedral opaque minerals (likely hematite based on the total oxide sum in the microprobe). Microprobe analysis shows that the late-stage serpentine veins (violet circles, Fig. 3c) are close to end-member Mg-serpentine ($Mg_3Si_2O_5(OH)_4$, lizardite, based on XRD analysis). Altered pyroxenes exhibiting bastite textures are composed of serpentine with elevated aluminum content (dark red, Fig. 3c) following solid solution vectors between Mg-serpentine and amesite ($Mg_2Al(AlSiO_5)(OH)_4$). The aluminum is likely inherited from the pyroxene precursor. The late-stage serpentine vein and bastite serpentine, which are clear to slightly translucent in the optical microscope, are poor in Fe (Fig. 3d). In contrast, serpentine mesh after olivine mostly has dark-colored cores (Fig. 3b) with higher Fe (Fig. 3d). The serpentine mesh is composed of a mixture of Mg-serpentine and ferrous-iron-bearing brucite (Fig. 3d). However, microprobe analyses of the dark-colored cores also include compositions that indicate other Fe-bearing minerals, specifically those containing ferric iron (e.g., hematite, magnetite, cronstedtite, and Fe-oxyhydroxides such as goethite and ferrihydrite). XRD analysis reveals one peak that is associated with goethite (Fig. S2). In addition, the high bulk Fe(III)/ΣFe ratio of the same sample (Kelemen et al., 2021) suggests that little ferrous iron remains in these oxidized samples. Further work is needed to identify the dark-colored minerals within serpentine mesh cores in these oxidized rocks. These mineral grains are likely less than a few microns, and thus would require high resolution transmission electron microscopy for definitive identification.

4.1.2. *Sulfidic serpentinites (30–150 m)*

Samples recovered below 30 m are dark green in colour, typical of serpentinized peridotite. Hand sample observation reveals a mesh texture after olivine, cut by several generations of veins. XRD analysis of a representative sample from this alteration zone shows that this section is mostly composed of lizardite serpentine, similar to the sample from the oxidized serpentinite zone (Fig. S2). However, in contrast to samples from the oxidized zone, a peak corresponding to tochilinite is observed in the sulfidic zone sample. Tochilinite ($6Fe_{0.9}S•5(Mg,Fe)(OH)_2$) is a mixed sulfide and hydroxide mineral commonly observed in carbonaceous chondrite meteorite matrices (Mackinnon and Zolensky, 1984). Tochilinite has also been observed in terrestrial serpentinites (Beard and Hopkinson, 2000; Organova et al., 1988), as well as in laboratory products of hydrothermal alteration of olivine (McCollom et al., 2024). The presence of tochilinite contributes to the optically dark thin sections that characterize this alteration zone (Fig. 4a). Upon closer inspection, optically dark minerals comprise the cores of mesh textures, which are then surrounded by clear to translucent rims (Fig. 4b). Backscatter electron microscopy images of optically dark mesh textures show that the inner cores are composed of denser minerals relative to those in the outer rims and surrounding veins (Fig. 4c). Elemental mapping using energy dispersive spectroscopy (EDS) indicates that the inner core is more enriched in Fe and S (Fig. 4d), and less enriched in Si and Mg (not shown) than the rim. The core is also slightly more enriched in Ni (Fig. 4d), Cl, Al, Ca, and Ti (not shown) than the rims. This is consistent with rim-core-rim line analysis using wavelength dispersive spectroscopy (WDS), as shown in Fig. S3.

Analysis of hundreds of spots in the thin section sample shown in Fig. 4 using WDS in the microprobe, reveals complex and heterogenous mixtures of serpentine, brucite, and sulfide (FeS). Normalized to seven oxygen atoms per formula units (apfu), WDS analysis shows two distinct trends in the sulfur-rich mesh alteration type. The first paragenesis (black circles in Fig. 4e) is relatively more enriched in S, involving mixtures between a Fe-bearing lizardite serpentine (2 Si per 7 O apfu:

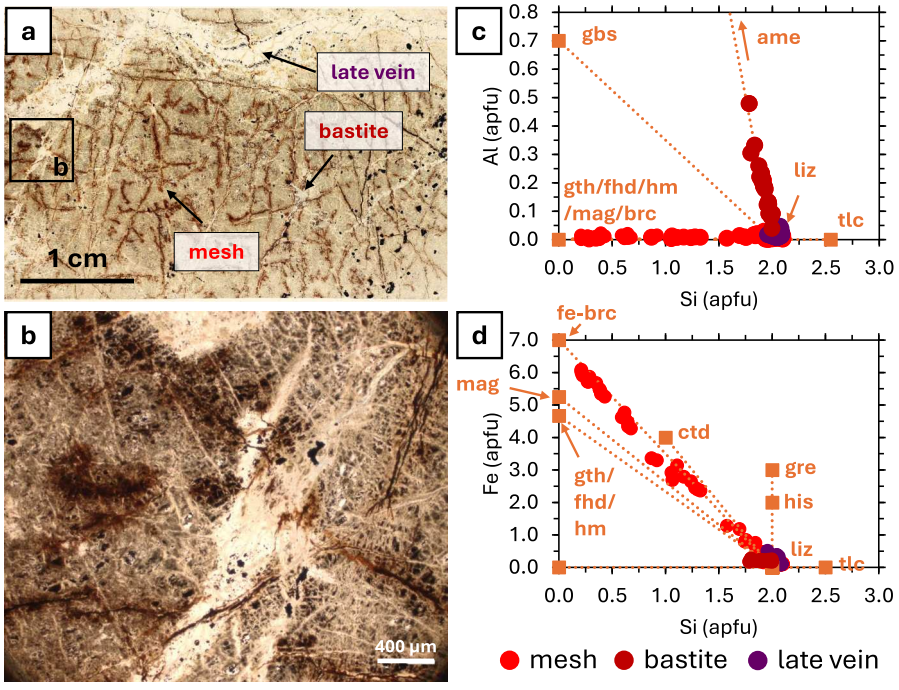

Fig. 3. Images and microprobe analysis of a representative sample from the oxidized serpentinite zone. (a) Whole thin section scan of a shipboard sample (BA1B_05_3_19_22.5 14 m depth) modified from Kelemen et al. (2020b). Labels in different colors indicate common alteration types in this zone. (b) Close up view of a portion of the whole thin-section scan, taken under a microscope using plane polarized light. (c) Al and Si atoms per formula unit (apfu), assuming seven oxygens, derived from microprobe data. (d) Fe and Si apfu, assuming seven oxygens, derived from microprobe data. Various shades of reds indicate alteration types shown in (a). Orange squares indicate mineral endmembers and dotted lines indicate mineral mixtures between indicated endmembers. Mineral abbreviations: gbs – gibbsite $Al(OH)_3$, ame – amesite $Mg_2Al_2SiO_5(OH)_4$, gth – goethite FeOOH, fhd – ferrihydrite $Fe(OH)_3$, hm – hematite Fe_2O_3, mag – magnetite Fe_3O_4, ctd – cronstedtite $Fe_4SiO_5(OH)_4$, gre – greenalite $Fe_3Si_2O_5(OH)_4$, liz – lizardite $Mg_3Si_2O_5(OH)_4$, tlc – talc $Mg_3Si_4O_{10}(OH)_2$, fe-brc – ferrous brucite $Fe(OH)_2$.

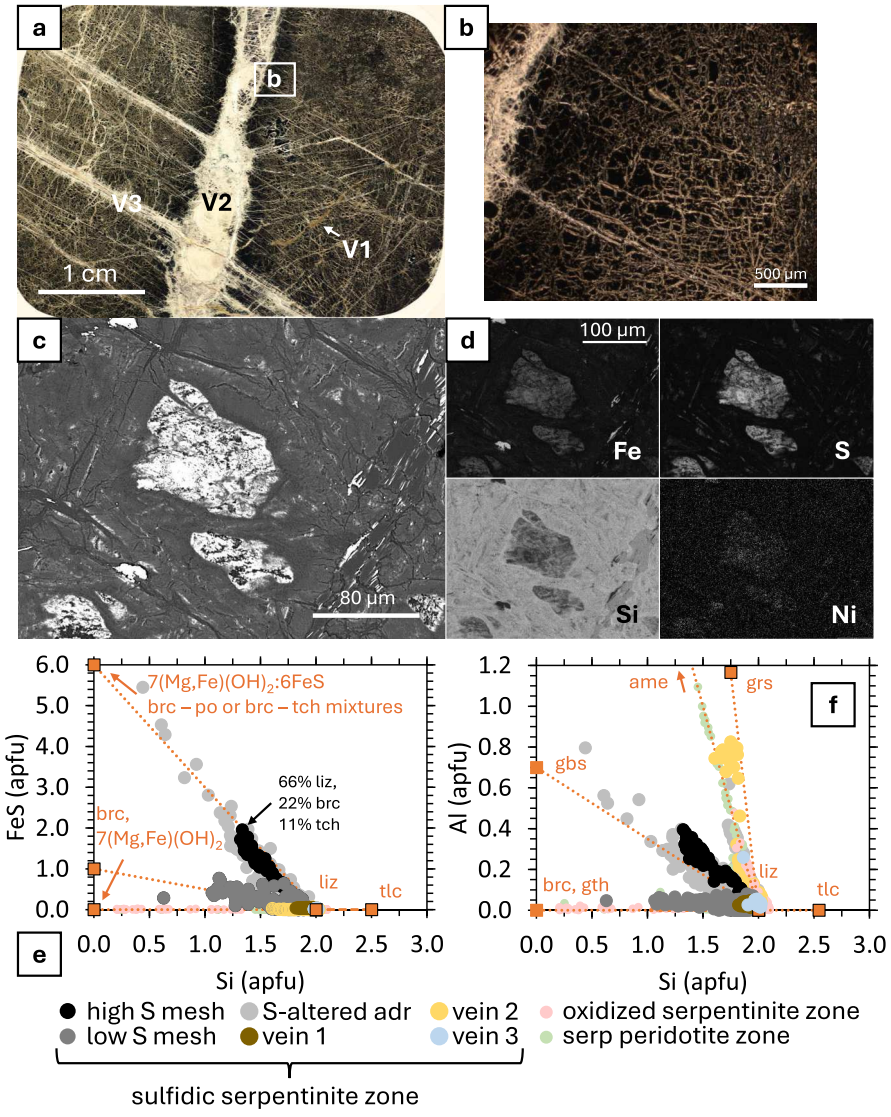

Fig. 4. Images and analysis of a representative sample from the sulfidic alteration zone. (a) Whole thin-section scan of a shipboard sample (BA1B_44_2_73_78 109 m depth), modified from Kelemen et al. (2020b). V1, V2, V3 denote different vein generations. (b) Close-up view of a portion of the whole thin-section scan, taken under the microscope using plane polarized light. (c) SEM backscattered electron image of a representative S-rich mesh alteration type. (d) SEM elemental maps via EDS showing locations in (c) that are enriched in Fe, S, Si, and Ni. The brighter spots are more enriched in these elements. (e) FeS and Si apfu, and (f) Al and Si apfu calculated from WDS data assuming 7-oxygen units. Orange squares indicate mineral endmembers and dotted lines indicate mineral mixtures between pairs of endmembers. Mineral abbreviations: brc - brucite $(Mg,Fe)(OH)_2$, po – pyrrothite (FeS), tch – tochilinite $(6FeS•5(Mg,Fe)(OH)_2)$, liz – lizardite $Mg_3Si_2O_5(OH)_4$, tlc – talc $Mg_3Si_4O_{11}(OH)_2$, gbs – gibbsite $Al(OH)_3$, ame – amesite $Mg_2Al_2SiO_5(OH)_4$, gth – goethite FeOOH, grs – grossular $Ca_3Al_2(SiO_4)_3$. (For interpretation of the references to colour in this figure legend, the reader is referred to the web version of this article.)

$(Mg,Fe)_3Si_2O_5(OH)_4$) endmember and a second endmember composed of brucite $(7(Mg,Fe)(OH)_2)$ plus pyrrhotite (6FeS, simplified version of $6Fe_{0.9}S$). Note that O in hydroxyl $(OH)^{-1}$ is conventionally counted as 0.5 O apfu, as only half of the −2 charge of O is balanced by EPMA-measurable cations (e.g., Ca^{+2}, Mg^{+2}, Si^{+4}, but not H^{+}). Stoichiometrically, this endmember is equivalent to a mixture of 2 mol of brucite and 1 mol of tochilinite $(2(Mg,Fe)(OH)_2 + 6FeS•5(Mg,Fe)(OH)_2$, altogether 7 oxygen apfu). Overall, the most S-enriched spot (Fig. 4e) within mesh-textured alteration assemblages corresponds to a combination of 67 mol % (~60 wt%) lizardite, 22 mol% (~10 wt%) brucite, and 11 mol% (~30 wt%) tochilinite. This combination contains ~10 wt% S, consistent with results of rim-core WDS analysis (Fig. S3).

The second mesh paragenesis is considerably less enriched in S (dark gray circles, Fig. 4e). This mesh is usually less optically dark than the first paragenesis when viewed in plane-polarized light. Spot WDS analyses indicate that relatively S-poor meshes are more enriched in lizardite and brucite, at the expense of tochilinite.

Compared to the second type, the more optically black, S-rich parageneses are also more enriched in Al (Fig. 4f). In addition to these two, a rarer S-rich alteration type is observed in the same thin section. This third assemblage exhibits the highest S content in the sample (light gray circles, Fig. 4e), and is also more enriched in Ca relative to most other spots in the thin section (Fig. S4). WDS spot analysis (Fig. S4a) suggested that this assemblage is a mixture of tochilinite, lizardite, (hydro)andraditic garnet $(Ca_3Fe_2(SiO_4)_{3-x}(OH)_{4x})$, and perhaps even portlandite $(Ca(OH)_2)$. The most Ca-rich spots in this assemblage are also the most Fe-rich (after accounting for and removing FeS), as shown in Fig. S4b. The trend of Ca and Fe in these data has a higher slope than that for mixtures including andradite and hydroandradite (slope of 1.5), perhaps due to the presence of portlandite.

Unlike the mesh, veins are not S-rich (light blue, yellow, and brown circles, Fig. 4e). This indicates that vein minerals are less prone to sulfidation than those originally present in the mesh cores. These veins are primarily composed of lizardite serpentine. V1 and V3 veins are

composed of almost pure Mg-lizardite. On the other hand, the composition of serpentine that comprises the large V2 vein is more diverse. The large V2 vein is a composite of several smaller veins cross-cutting each other. It has 1.5 to 2 Si atoms per 7 O atoms, suggesting that it is a submicroscopic mixture of serpentine and brucite (Fig. 4e). Some V2 veins are enriched in Al, plotting along the lizardite-amesite trend (Fig. 4f), perhaps including some (hydro)andradite-grossular garnets. The chemical trends in this vein are similar to those in bastite textures in the oxidized zone (Fig. 3c) as well as some of the late-stage "waxy" veins observed in Holes BA1B and BA4A (Kelemen et al., 2021).

4.1.3. Serpentinized peridotite (150–400 m)

Alteration textures in cores recovered from depths deeper than 150 m in Hole BA1B are similar to those commonly observed in serpentinized peridotites from around the world (e.g., Evans, 2004; Frost et al., 2013; O'Hanley, 1992; Wicks and Whittaker, 1977). In most cases, relict olivine is observed, rimmed by serpentine and brucite, exhibiting initial stages of mesh and hourglass texture formation (Evans, 2004; Wicks and Whittaker, 1977). In some mm-scale areas (Fig. 5a) olivine is completely altered to serpentine and brucite in a mesh texture. Orthopyroxene is altered to form bastite pseudomorphs, as is typical for serpentinites (Wicks and Whittaker, 1977). Spot WDS analyses show that bastite textures are composed of a mixture of lizardite and amesite (Fig. 5b). In contrast, secondary minerals surrounding olivine, and the cores of mesh pseudomorphs, are mostly composed of serpentine and brucite mixtures.

4.1.4. Nanoscale observation

A FIB cross-section encompassing olivine altered into a mixture of serpentine and brucite (WDS-derived Mg + Fe/Si ratio between 1.6 and 1.8) was examined for nanoscale alteration textures and compositions (Fig. 6a). The sample was collected from a partially serpentinized peridotite located near a H_2-rich hyperalkaline spring in the Samail ophiolite (Al Bana, Leong et al., 2021) to investigate incipient stages of olivine serpentinization. Results, shown in Fig. 6b–d, indicate the presence of tochilinite. Several dark bands, indicating relatively dense materials under brightfield (BF) imaging, are present in the alteration assemblage replacing olivine (Fig. 6b). EDS mapping shows that these dark bands are more enriched in S and Fe and depleted in Si relative to surrounding alteration phases (Fig. 6b). Upon closer inspection, these dark bands are surrounded by lizardite layers (characterized by 7 Å lattice spacing), as shown in Fig. 6c. Lizardite is commonly observed in previous TEM studies of serpentinites (Andreani et al., 2007; Dódony and Buseck, 2004; Evans et al., 2013). High resolution imaging (Fig. 6d) and Fast Fourier Transform (FFT) analyses of these dark bands under BF reveal that each layer spacing is ~10.8 Å. This lattice spacing as well as the EDS analysis corroborate the presence of tochilinite. Tochilinite observed in this work has similar lattice spacings as those examined from meteorites (Mackinnon and Zolensky, 1984), interplanetary dust particles (Bradley and Brownlee, 1991), and terrestrial samples (Organova et al., 1988). Intergrowth of tochilinite and serpentine replacing olivine indicates that tochilinite formation can occur even in the incipient stages of mesh pseudomorph formation. Continuous supply of sulfur as alteration progresses may produce sulfidic rocks such as those observed in Hole BA1B.

4.1.5. Nickel trends in BA1B

The bulk Ni contents of rocks recovered from BA1B are approximately constant (Kelemen et al., 2020a, also see Fig. 1) and similar to bulk Ni concentrations of peridotites throughout the Samail ophiolite (2000–2600 ppm Ni, e.g., Godard et al., 2000; Hanghøj et al., 2010; Monnier et al., 2006). In this work, we show that the distribution of Ni in the various secondary minerals observed in BA1B is heterogenous at a thin-section, probably even submicron, scale. The NiO and ΣFeO contents (in wt%) of secondary minerals in BA1B, as measured via WDS spot analysis, are shown in Fig. 7a. There is no clear relationship between the Ni and Fe content of sample targets when all analyses are considered together. However, there are clear trends when some alteration types are examined independently. In the oxidized serpentinite zone (0–30 m), the highest Ni content is found in the most Fe-enriched spots (light red circles in Fig. 7a). These spots correspond to those that are enriched in oxyhydroxides relative to serpentine. In these spots, Ni is likely bound structurally inside oxyhydroxides by substituting for Fe in Fe—Ni oxyhydroxide solid solutions or sorbed at Fe-oxyhydroxide surfaces. The NiO content of some spots exceeds 1 wt%, comparable to those in nickeliferous limonite (i.e., Fe-oxyhydroxide-rich) horizons in laterite deposits (Gleeson et al., 2003).

In the sulfidic serpentinite zone (30–150 m), the Ni content increases with S content along different trends for high-S mesh (black circles) versus low-S mesh (dark gray circles) versus S-altered andradite (light gray circles, Fig. 7b). These three trends suggest mixing between lizardite and possible tochilinite-bearing endmembers. For the low-S mesh (dark gray circles, Fig. 7b), the tochilinite-bearing end-member (tch_1 in Fig. 7b) is $6(Fe_{0.9}Ni_{0.1})S*5(Mg_{0.8}Fe_{0.2})(OH)_2$, which is a mixture between a tochilinite ($6FeS*5(Mg_{0.8}Fe_{0.2})(OH)_2$) and haapalaite (4(Fe,Ni)

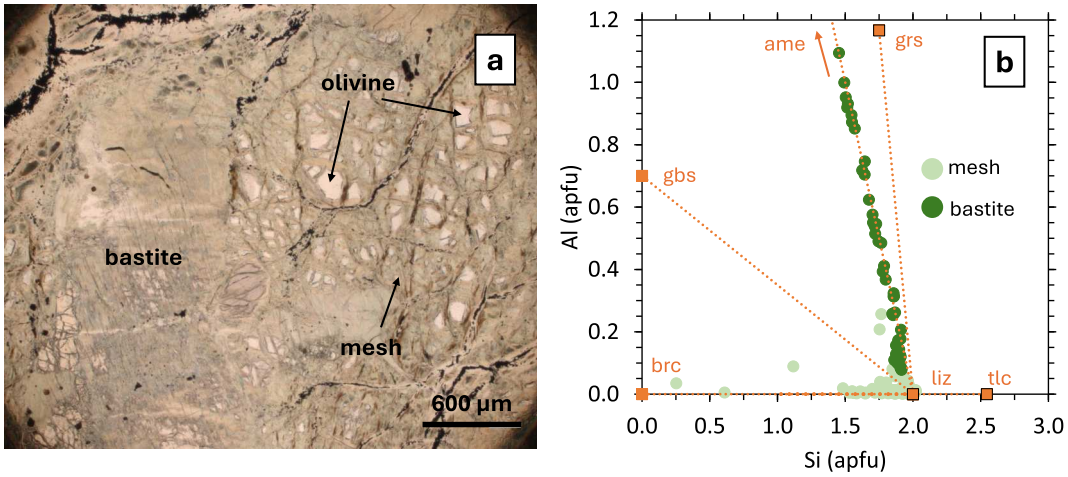

Fig. 5. Image and microprobe analyses of a representative sample from the partially serpentinized peridotite zone below 150 m. (a) A plane polarized microscope image showing a portion of the whole thin-section scan depicted in Fig. 2 (BA1B_114_4_51_56 321 m depth). Relict olivine and two main alteration types or textures (mesh and bastite) are indicated in black letters. (b) Al and Si apfu calculated from microprobe data, assuming 7 oxygen units. Orange squares indicate mineral endmembers and dotted lines indicate mineral mixtures between pairs of endmembers. Mineral abbreviations: brc - brucite $(Mg,Fe)(OH)_2$, liz – lizardite $Mg_3Si_2O_5(OH)_4$, tlc – talc $Mg_3Si_4O_{11}(OH)_2$, gbs – gibbsite $Al(OH)_3$, ame – amesite $Mg_2Al_2SiO_5(OH)_4$, grs – grossular $Ca_3Al_2(SiO_4)_3$.

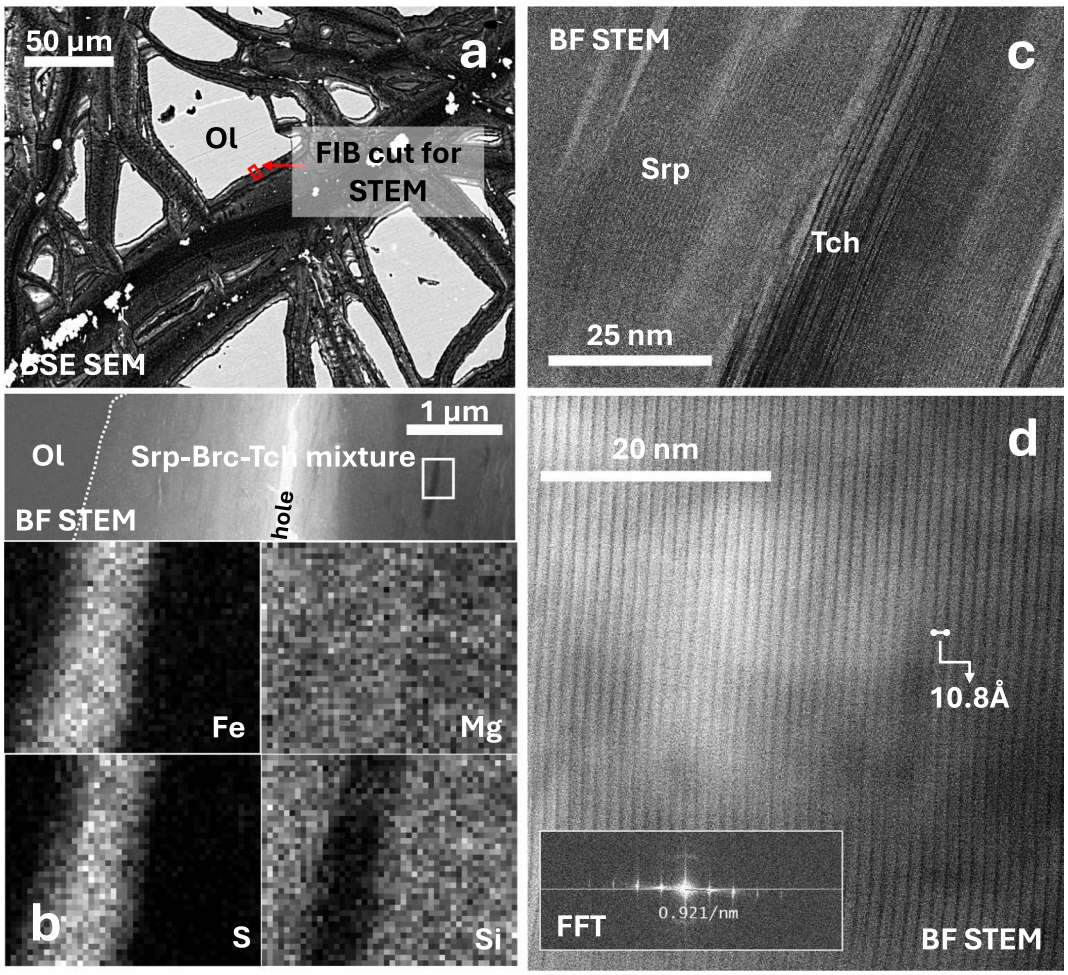

Fig. 6. Results of Scanning Transmission Electron Microscopy (STEM). (a) BSE image showing location of the cross-section cut by the FIB for STEM analysis. (b) Brightfield (BF) STEM image (200 kV accelerating voltage) of an olivine (Ol) altering into a mixture of serpentine (Srp), brucite (Brc), and tochlinite (Tch). Dotted line denotes boundary between olivine and the alteration assemblage. EDS chemical maps for Fe, Mg, S and Si were obtained from the region shown in the white square. (c) Another BF image (200 kV) showing dark denser minerals (tochilinite) surrounded by lighter-colored lizardite layers. (d) BF STEM view of another and larger dark band showing layers with 10.8 Å spacing. Lattice spacing is supported by Fast Fourier Transform (FFT) pattern analysis of the high-resolution image that indicates 0.921/nm or 10.8 Å spacing.

S•3(Mg,Fe)$(OH)_2$). The second (tch_2, $6(Fe_{0.98}Ni_{0.02})S*5(Mg_{0.8}Fe_{0.2})(OH)_2$) and third ($tch_3$, $6(Fe_{0.99}Ni_{0.01})S*5(Mg_{0.8}Fe_{0.2})(OH)_2$) tochilinite-bearing endmembers, corresponding to high S mesh and S-altered andradite spots, respectively, have lower haapalaite components (lower Ni/Fe and Ni/S). Veins in the sulfidic zone are poor in S (blue and yellow symbols, Fig. 7b), but they can be as enriched in Ni as the mesh.

In the deeper serpentinized peridotite zone (150–400 m), relict olivine contains ~0.35 to 0.5 wt% NiO (green diamonds, Fig. 7), consistent with the typical Ni content of olivine in Samail ophiolite outcrop samples (Falk and Kelemen, 2015; Hanghøj et al., 2010; Khedr et al., 2014; Monnier et al., 2006). The Ni content of serpentine in this deeper zone varies. NiO in bastite is particularly low (typically, <0.15 wt%). However, locally there is >1 wt% NiO in serpentine-brucite mesh mixtures. The mesh assemblages in this zone do not have significant S contents. Instead, it is likely that Ni in these assemblages is hosted in hydroxides (e.g., towards theophrasite or $Ni(OH)_2$ endmember), serpentine (e.g., towards nepouite or $Ni_3Si_2O_5(OH)_4$ endmember) or in nanoscale awaruite (Ni_3Fe, Ellison et al., 2021).

Overall, while there are spots in each alteration zone that are more enriched in Ni than relict olivine (green diamonds, Fig. 7) and bulk Samail ophiolite peridotites (green band, Fig. 7), there are other alteration types that are more depleted in Ni. Thus, overall, no systematic Ni enrichment in bulk samples is observed as a function of depth in Oman Drilling Project cores (Kelemen et al., 2020b, 2020d, 2020e).

4.2. *Thermodynamic simulations*

Thermodynamic reaction-path calculations were conducted to simulate irreversible mass transfer reactions during reaction of Oman serpentinites with meteoric-derived groundwater. Simulations are divided into two steps. The first step of the calculations simulates interaction of average Oman serpentinized harzburgite and dunite compositions with rain-derived groundwater in a system open to atmospheric exchange, representative of the shallow, oxic aquifer in the Samail ophiolite (e.g Kelemen et al., 2021; Leong et al., 2021; Nothaft et al., 2021a; Rempfert et al., 2023). In contrast, the second step of the calculations simulates conditions when shallow groundwater percolates deeper into the aquifer. Deeper groundwater reacts with the same serpentinite rock compositions used in the first step, but in systems closed to atmospheric input. Overall, the first and second steps model groundwater interactions with the same serpentinized lithologies at different depths.

4.2.1. *Open system shallow alteration*

The evolution of fluid and secondary mineral compositions during reaction of a representative Oman serpentinized dunite with global

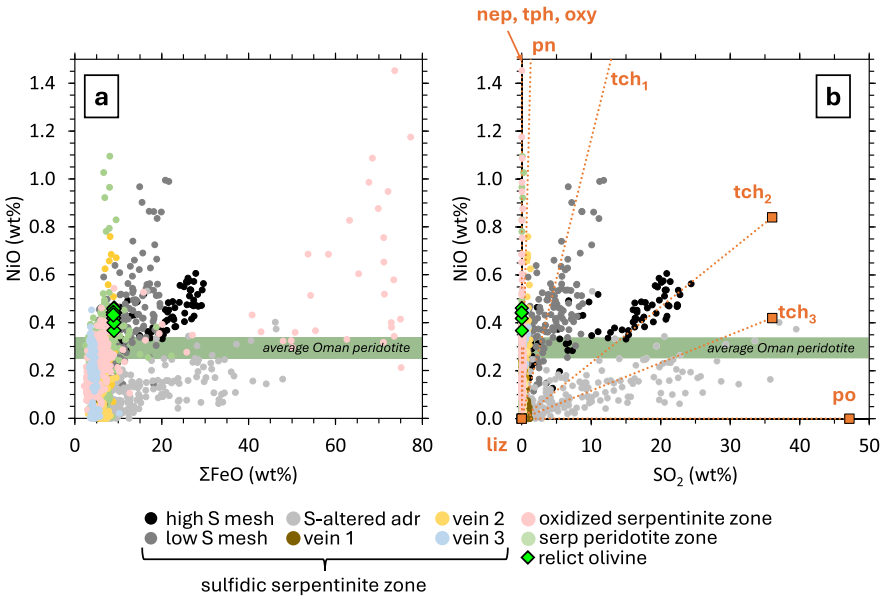

Fig. 7. Nickel contents of spots in the three thin sections shown in Figs. 3, 4, and 5. (a) Ni (as wt% NiO) and Fe (as wt% FeO). (b) Ni (as wt% NiO) and S (as wt% SO_2) contents. Green bands indicate ranges in the NiO content of typical Oman peridotites (Hanghøj et al., 2010). Mineral abbreviations: nep – nepouite $Ni_3Si_2O_5(OH)_4$, oxy – nickel oxyhydroxide NiOOH or $Ni(OH)_3$, tph – theophrasite $Ni(OH)_2$, pn – pentlandite $Ni_{4.5}Fe_{4.5}S_8$, po – pyrrhotite FeS, tch – Ni-bearing tochilinite solid solution. See text for the composition of the three representative tochilinite-bearing endmembers. (For interpretation of the references to colour in this figure legend, the reader is referred to the web version of this article.)

average rainwater is shown in Fig. 8a and b. Model outcomes are plotted as a function of the water:rock ratio, increasing from left to right in these diagrams, simulating increasing extents of interaction of a given mass of serpentinized dunite with meteoric-derived fluids. A water:rock ratio of 1000 results from reaction of 1 kg of serpentinized dunite with 1000 kg of meteoric water. The simulation is open to atmospheric input. Thus O_2 and CO_2 consumed by water:rock reactions are replenished to maintain equilibrium with the atmosphere.

Starting with acidic rain (pH ~5.6), the pH of the reacting fluid is buffered to about 8.5 when the water:rock ratio is less than 10,000, that is, when 1 kg of serpentinized dunite has reacted with at most 10,000 kg of percolating groundwater. This pH is consistent with observed pH in shallow wells and surface runoff in the Samail ophiolite. These fluids, also known as Type I Mg^{+2} and HCO_3^- fluids (Barnes and O'Neil, 1969), closely align with model results shown in Fig. 8a, where dissolved Mg (mostly speciated as Mg^{+2}, gray curve, Fig. 8a) and inorganic C (mostly speciated as HCO_3^-, light blue curve) dominate solutes in fluids at water:rock ratios <10,000. Concentrations reach values of ~1 mmolal for these two dissolved species, similar to observed groundwater and stream water in Oman (Canovas et al., 2017; Chavagnac et al., 2013; Dewandel et al., 2005; Howells et al., 2022; Leong et al., 2021; Matter et al., 2006; Miller et al., 2016; Neal and Stanger, 1985; Nothaft et al., 2021a, 2021b; Paukert et al., 2012; Paukert Vankeuren et al., 2019; Rempfert et al., 2017, 2023). Dissolved Ca and Si concentrations are tens of micromolal, also close to or slightly lower than those observed in field samples. Simulation results show that total dissolved S (ΣS, mostly speciated as SO_4^{-2}, orange curve in Fig. 8a) increases when the water:rock ratio is <10,000. At a water:rock ratio of ~10, the dissolved sulfate concentration is ~1 mmolal, similar to concentrations measured in Type I fluids in Oman (Leong et al., 2021; Paukert et al., 2012). We terminated the simulations at this point, and modeled percolation of the produced fluid deeper into the aquifer in a system closed to atmospheric input, as discussed in the next section.

When the Samail serpentinized dunite has reacted with >100,000 kg of meteoric-derived fluid in this simulation, it is completely altered into an assemblage dominated by iron oxyhydroxide (red curve, Fig. 8b) and serpentine (green curve). The serpentine solid solutions precipitated at these high water:rock ratios is rich in ferric iron (i.e., hisingerite, $Fe(III)_2Si_2O_5(OH)_4$). Moreover, our simulations show that most of the Ni remains in the rocks at water:rock ratios <500,000 (dashed gray curve in Fig. 8b). The Ni content of the secondary assemblages accumulates to more than 1.1 wt% in the iron oxyhydroxide + ferric serpentine secondary assemblage that forms at water:rock ratios between 100,000 and 500,000. This extent of Ni accumulation is typical of limonite or oxyhydroxide-rich horizons found in nickeliferous laterite deposits replacing ultramafic rocks (Gleeson et al., 2003). At water:rock ratios below 10,000, the Ni content of the rock remains at values similar to the protolith dunite (0.2 wt% Ni). Most of the Ni stays in the rocks, together with the other major elements (e.g., Mg, Si), mostly hosted in serpentine (green curve, Fig. 8b) with minor talc (blue-green curve) and carbonates (violet curve). As a consequence, the Ni content of the resulting mineral assemblage is lower than those at water:rock ratios >10,000. The model-predicted ΣS content of the bulk solid product remains at zero (black dashed curve in Fig. 8b). All the sulfur from the serpentinized dunite protolith (assumed as 300 ppmw) is mobilized into the fluid as dissolved sulfate. No sulfur-bearing minerals are precipitated in the step 1 models. We also conducted simulations assuming that the composition of the reacting protolith is equivalent to a representative Samail ophiolite serpentinized harzburgite. Results of simulations are shown in Fig. S5. Model results are similar to those described above for the model serpentinized dunite.

4.2.2. *Closed system deep alteration*

In the second step of our model simulations, we allow reaction of the fluid yielded by the simulation described in the previous section (i.e., product fluid at water:rock ratio of 10) with representative Samail ophiolite serpentinized dunite (the same protolith as in the previous section). However, the model system is now closed to atmospheric input, to simulate percolation of shallow groundwater to deeper aquifers. Thus, dissolved O_2 and inorganic carbon (ΣCO_2) that are consumed during mineral oxidation and carbonation reactions would not be replenished as reaction progresses. Results of this simulation are shown in Fig. 9.

When each 1000 kg of percolating groundwater (starting pH ~8.5) reacts with more than 1 kg of representative Oman serpentinized dunite (water:rock ratio of <1000, Fig. 9a), the fluid pH starts to increase, attaining values >11 at water:rock ratios <20. In addition, dissolved Mg

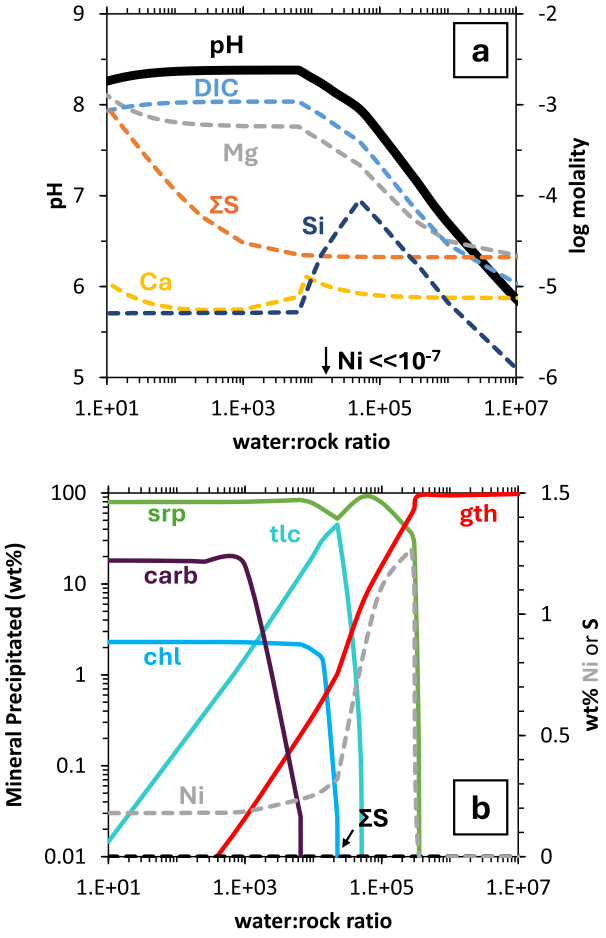

Fig. 8. Thermodynamically predicted evolution of the composition of fluids (a) and solids (b) during reaction of Oman serpentinized dunite with meteoric-derived groundwater at 35 °C and 50 bars, and open to atmospheric input (Step 1 calculation, modified from Step 1 in Fig. 29, Kelemen et al., 2021). The pH (solid black line in (a)) changes from that of rain (~5.6 on the right) to alkaline values (pH ~8.5 on the left) as more rocks are reacted in a given mass of percolating, meteoric-derived groundwater. Dashed curves in (a) indicate evolution of dissolved species. The acronym "DIC" refers to dissolved inorganic carbon (typically dissolved CO_2, bicarbonate, or carbonate ions and their complexes). Dissolved Ni concentrations remain very low throughout the reaction path. Solid curves in (b) indicate mineral proportions (in wt%) of solid products, which are predominantly composed of serpentine and – at very high water:rock ratio – goethite. The dashed gray curve indicates the Ni content (in wt% Ni) of the combined solid product, showing the water:rock ratios required for Ni enrichment to occur. The solid product has 0 wt% S, due to total mobilization of S into the fluid phase. Mineral abbreviations: serp -serpentine, gth – goethite, tlc – talc, chl – chlorite. carb – carbonates (sum of all carbonate precipitates: magnesite, calcite, dolomite).

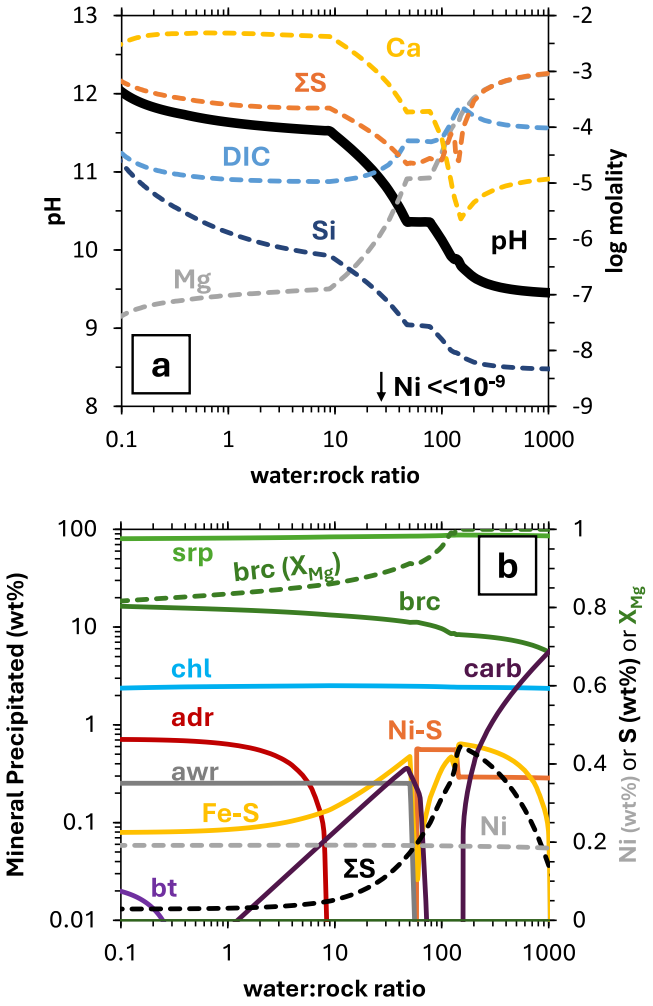

Fig. 9. Thermodynamically predicted evolution of the composition of fluids (a) and solids (b) during reaction of Oman serpentinized dunite with groundwater at 35 °C and 50 bars, and closed to atmospheric input (Step 2 calculation, modified from Step 2 in Fig. 29, Kelemen et al., 2021). The pH (black curve in (a)) increases to hyperalkaline values (>11) as the water:rock ratio decreases. Dissolved Ni concentration remains very low. The solid products are predominantly serpentine, but include several other minerals, as shown in (b). Black and gray dashed curves in (b) indicate evolution of the S and Ni content of the solid products. The dashed dark green curve shows the X_{Mg} of the precipitated brucite. Mineral abbreviations: srp – serpentine, brc – brucite, chl – chlorite, adr – andradite, awr – awaruite, bt – biotite, carb – carbonates (sum of all carbonate precipitates: magnesite, calcite, dolomite), Ni—S – nickel sulfide (sum of millerite and pentlandite), Fe—S – iron sulfide (sum of pyrite and pyrrhotite). (For interpretation of the references to colour in this figure legend, the reader is referred to the web version of this article.)

concentrations decrease to <1 μmolal while dissolved Ca contents increase to >1 mmolal. These concentrations are consistent with those measured from deep-seated hyperalkaline ground and spring water in Oman (Dewandel et al., 2005; Leong et al., 2021; Neal and Stanger, 1985; Nothaft et al., 2021a; Paukert et al., 2012; Paukert Vankeuren et al., 2019; Rempfert et al., 2017). These fluids are typically called Type II Ca^{+2}-OH^{-} water (Barnes and O'Neil, 1969). Model-predicted Si and dissolved inorganic C concentrations (at most 10 μmolal, Fig. 9) are close to those measured from endmember hyperalkaline fluids in Oman (Leong et al., 2021).

Predicted secondary minerals that form after reaction of percolating groundwater with the representative Oman serpentinized dunite are shown in Fig. 9b. Sulfide minerals precipitate at water:rock ratios between 1000 and 10 (orange curves in Fig. 9b), causing a drop in the total dissolved S (orange curve in Fig. 9a). For the Ni sulfides (brown curve, Fig. 9b), millerite (NiS) predominates at water:rock ratios between 1000 and 100, while pentlandite ($Fe_{4.5}Ni_{4.5}S_8$) is favored at lower water:rock ratios (100 to 50). At even lower water:rock ratios (<50), Ni sulfides are not predicted to form. Instead, most of the Ni in the solid assemblage is hosted in awaruite (Ni_3Fe, dark gray curve in Fig. 9b). Among the Fe-sulfides (orange curve in Fig. 9b), pyrite (FeS_2) predominates at a water:rock ratio greater than 100, while troilite (FeS, as an approximation to pyrrhotite's $Fe_{0.9}S$) is predicted to form at water:rock ratios less than 100. Altogether, precipitation of these sulfide minerals facilitates mass transfer of S from fluid to solid. Most of this occurs at water:rock ratios between 1000 and 10, corresponding to the steep drop in

total dissolved sulfur concentration (orange curve, Fig. 9). Calculations show that in this range of water:rock ratio, the total secondary mineral precipitates can have up to 0.45 wt% S (dashed black curve in Fig. 9b). This process may account for the S-rich zones in Holes BA1B and BA4A. At water:rock ratios lower than 10, the ΣS content of the mineral precipitates is <0.05 wt%, due to dilution with an increasing mass of solid precipitates (e.g., serpentine and brucite) as more and more of the protolith reacts with a given mass of percolating groundwater. Towards lower water:rock conditions, brucite increasingly becomes more iron-rich, as shown by the decreasing X_{Mg} (Mg/(Mg + Fe) ratio) trend for brucite (dashed dark green curve in Fig. 9b).

While S can accumulate in the precipitating solids in a specific range of water:rock ratio, the Ni content of the solids remains approximately constant at all water:rock ratios. The Ni content remains at ~0.19 wt%, equivalent to that of the protolith (dashed gray curve in Fig. 9b). We also conducted simulations of reaction with serpentinized harzburgite. Results, depicted in Fig. S6, show trends similar to those described above for a serpentinized dunite protolith, except that less brucite forms due to the higher Si content of harzburgite compared to dunite. The ΣS content of precipitated mineral assemblages reaches 0.39 wt%, slightly lower than that in the dunite alteration scenario.

Simulations were continued at water:rock ratios lower than 0.1, but are not shown in Figs. 8 and S6. At these rock-dominated conditions, water is rapidly consumed by mineral hydration reactions. At a water:rock ratio of 0.05 (i.e., reaction of 20 kg of the model protoliths with one kg of percolating groundwater), consumption of water is almost complete. The reaction of water with protoliths that are fresher (i.e., less serpentinized) will lead to complete consumption of water at higher water:rock ratios. For completely fresh ultramafic reactants (~0 % H_2O), very little of a groundwater reactant remains at water:rock ratios lower than 0.2 (i.e., reaction of 5 kg of protolith for every kg of groundwater, Leong et al., 2021; Leong and Shock, 2020).

5. Discussion

5.1. A supergene style enrichment of sulfur in BA1B

Results of models described in the previous section indicate that sulfur enrichment can occur even at conditions (35 °C, 50 bars) consistent with the pressure and temperature of ambient groundwater in the OmanDP Multi-Borehole Observatory (MBO). Under the oxic conditions imposed by Earth's atmosphere, sulfur accumulates in circulating shallow groundwater, as depicted in the simulation results shown in Fig. 8a. Sulfur present in the protolith (fresh to serpentinized peridotite), likely occurring in sulfide minerals with oxidation states ranging from S^{-2} to S^{-1}, is mobilized into the fluids as mineral reactants are oxidized. In the fluid phase, dissolved sulfur is mainly in sulfate (SO_4^{-2}, oxidation state is S^{+6}) and remains dissolved because the model fluid remains undersaturated relative to sulfate minerals. This is consistent with the compositions of Type I and II fluids sampled from the Oman ophiolite, which are far below anhydrite saturation (Leong et al., 2021). Some pH >11 hyperalkaline fluids from the Troodos ophiolite are much more enriched in dissolved SO_4^{-2} relative to those in the Oman ophiolite (<0.1 mmolal), attaining concentrations >5 mmolal SO_4^{-2} (Evans et al., 2024; Neal and Shand, 2002). However, these relatively SO_4^{-2}-rich fluids are still undersaturated with respect to sulfate minerals (Neal and Shand, 2002). Overall, sulfur can accumulate in circulating oxic, shallow groundwater, stripping the shallow host rocks of sulfur. When these oxic fluids percolate deeper into the aquifer, S can be reprecipitated and accumulate as serpentinization of protolith serpentinites (either serpentinized dunites or harzburgite) drastically reduces fO_2 in reacting groundwater. The reacting ultramafic rock does not need to be fresh (i.e., olivine). Instead, ongoing alteration of serpentinized lithologies can still produce alkaline, reduced fluids (Kelemen et al., 2021; Leong and Shock, 2020). Specifically, serpentine and brucite containing ferrous iron are still predicted to be oxidized to ferric iron bearing serpentine, oxides (e.g., magnetite) and oxy-hydroxides (Ellison et al., 2021; Ely et al., 2023; Kelemen et al., 2021; Templeton et al., 2024; Templeton and Ellison, 2020; Tutolo et al., 2020).

Model results shown in Figs. 8 and 9, depicting open shallow and closed deep aquifer conditions, respectively, are summarized in Fig. 10. Overall, the following scenarios are proposed to form the S-enriched layer observed in drill core from Hole BA1B. The water:rock ratio shown in Fig. 10 accounts for the integrated mass of rock that had reacted in both open oxic and closed reduced steps in the simulations. The evolution of the H_2 (aH_2) and H_2S (aH_2S) activities as percolating groundwater reacts with dunite is plotted in an activity diagram (black solid curve in Fig. 11; dotted curve depicts harzburgite reactant). Fig. 11 also depicts the stabilities of relevant Fe-sulfide, Ni-sulfide, Fe-oxide, and alloy minerals.

(1) First, S is leached from the solid reactants during oxic weathering of shallow aquifer rocks (Fig. 10, red background). This is facilitated by continuous atmospheric input, buffering the fluid to the high fO_2 conditions that are required to mobilize sulfur as dissolved sulfate. The altered rocks produced by weathering are oxidized (Fe-oxyhydroxide to serpentine dominated, see Fig. 8b), with 0 wt% ΣS (Fig. 10c). Dissolved sulfate reaches ~1 mmolal at a water:rock ratio of ~10 (Fig. 10b). This fluid product has pH of ~8.5 (Fig. 10a), and redox conditions buffered by Earth's atmosphere (log $fO_2 = -0.67$, log aH_2 and log $aH_2S << -10$, Fig. 10c and d).

(2) In a second alteration step, these oxic, sulfate-bearing, slightly alkaline fluids percolate deeper into the aquifer where atmospheric input is minimal. In this setting, oxic species such as dissolved O_2 and CO_2 are consumed via mineral oxidation and carbonation, respectively, without being resupplied by the atmosphere. Without O_2, ferrous iron in the protoliths is oxidized into ferric iron, eventually reducing some H_2O to form dissolved H_2. The increase in the activity of dissolved H_2 (aH_2) or the hydrogen fugacity (fH_2), and the corresponding decrease in the oxygen fugacity (fO_2), favors reduction of sulfate to sulfide. Thus, aH_2S increases as fluids become more H_2-rich. This stabilizes Fe-sulfides and some Ni-sulfides relative to oxide minerals (Fig. 11). The sulfidic serpentinite zone occurs where the aH_2S is high, precipitating Fe-sulfides such as pyrite and pyrrhotite (or tochilinite), and Ni-sulfides such as millerite and pentlandite (Fig. 11). In our simulations, several sulfide minerals are predicted to precipitate, causing a dramatic drop in the dissolved sulfate concentration of the percolating groundwater (Fig. 10b, gray background). Most of the dissolved S is precipitated in sulfide minerals, producing solid mineral assemblages containing up to 0.45 wt% ΣS (Fig. 10c). At water:rock ratio ~ 10, when fluid starts to become reduced, most of the sulfur is precipitated in pyrite and millerite. As fluids become even more reduced, at lower water:rock ratios, pyrrhotite and pentlandite are favored. The formation of brucite is also predicted in the models. Thermodynamic data for tochilinite is insufficient, and hence this mineral was not included in our models. As in the interpretation of meteorite alteration models (Neveu et al., 2017), we interpret the co-occurrence of brucite and pyrrhotite in our models to be equivalent to formation of tochilinite, which is compositionally similar to 5:6 mole mixture of brucite and pyrrhotite or troilite, respectively. As shown by the dashed dark green curve in Fig. 9b (X_{Mg} of brucite solid solution), brucite at these ranges in water:rock ratio is indeed more Mg-rich than brucite precipitated at lower water:rock ratios where the bulk rock S content is low. Overall, mineral parageneses depicted from left to right in Fig. 9b show that a serpentinized dunite becomes less brucite-rich and more sulfide-rich as it encounters more and more S-bearing fluid (i.e., increasing water:rock ratio).

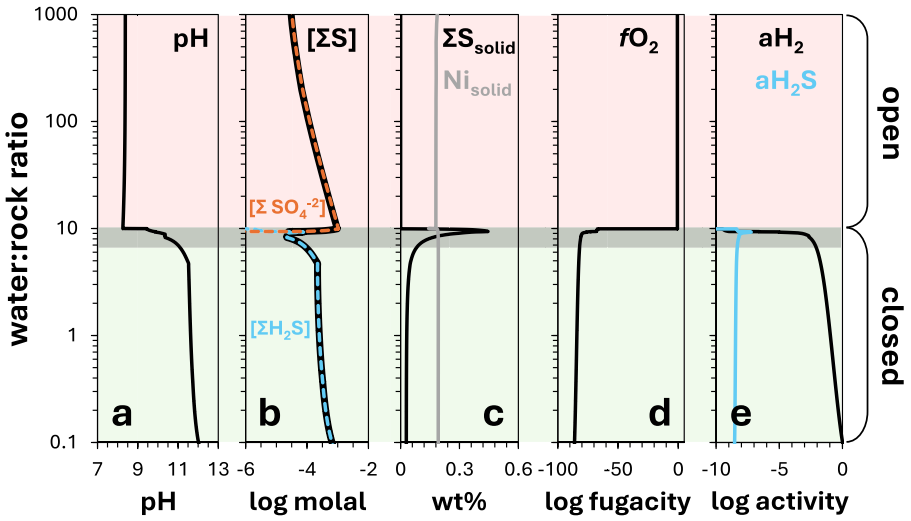

Fig. 10. Summary of Step 1 and 2 model results from Figs. 8 and 9. From left to right, trends depicted are the evolution of the pH, dissolved total sulfur concentration (in log molality, broken down into its oxidized and reduced components as total dissolved sulfate and sulfide ($\Sigma H_2S = H_2S + HS^-$), respectively), the S and Ni content of solid products in wt%, the oxygen fugacity (fO_2), and the activities of dissolved hydrogen (aH_2) and sulfide (aH_2S) of the coexisting fluid. The water:rock regime with the red background is modeled in Step 1 calculations. The regime with the green background depict results from Step 2 models. (For interpretation of the references to colour in this figure legend, the reader is referred to the web version of this article.)

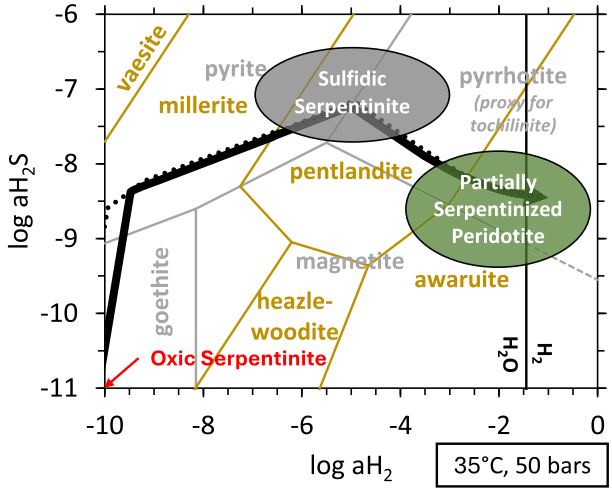

Fig. 11. The serpentinized dunite reaction path (solid black curve) depicted in Fig. 9, shown here in a dissolved hydrogen (aH_2) and sulfide (aH_2S) activity diagram at 35 °C and 50 bars. The dotted black curve is the reaction path for serpentinized harzburgite in Fig. S6. The different stability fields and phase boundaries between relevant minerals in Fe-O-H-S (gray lines) and Fe-Ni-O-H-S (gold lines) systems are also shown. Names of minerals are indicated in gray and gold letters, respectively. Approximate redox conditions (aH_2 and aH_2S) where each of the three alteration zones explored in this work (oxidized serpentine, sulfidic serpentine, and partially serpentinized peridotite) are indicated. Solid vertical line at the right side of the diagram depicts the phase boundary between H_2O and H_2 at 50 bars partial pressure of H_2. (For interpretation of the references to colour in this figure legend, the reader is referred to the web version of this article.)

While most of the sulfur is precipitated into minerals, a small proportion remains in the fluid as dissolved sulfide, mainly speciated as bisulfide (HS^-), instead of H_2S at alkaline conditions. The stability of dissolved S species prevents degassing of SO_2 or H_2S, even in the S-enriched zone. The loss of communication with the atmosphere also allows the pH of the fluid to increase to hyperalkaline levels (pH >11, Fig. 10c) due to continuous dissolution of Ca from the protoliths. Rapidly declining dissolved inorganic carbon concentrations (Fig. 9a, light blue curve) are not sufficient to precipitate calcium in solid carbonate minerals. Instead, Ca accumulates in the increasingly alkaline fluid (Fig. 9a, yellow curve).

Following Kelemen et al. (2021), the mass of weathered materials that provided the S in the sulfidic serpentinite zone in BA1B can be estimated. The sulfidic zone in BA1B is at least 6 times more enriched in total sulfur relative to an average Oman peridotite (~300 ppm S, or 0.03 wt%), assuming an average ΣS content of 0.2 wt% between 30 and 150 m. Therefore, if the transport of reacting fluid is diffuse and vertical, leaching of S following the oxidative weathering of ~700 m thick peridotite can account for the 120 m thick sulfidic zone. For this scenario, since the sulfidic zone is only 50 m below the surface, we infer that S was leached from ~650 m of peridotite that has since eroded away. Alternatively, the required peridotite source layer can be much thinner, if groundwater tends to migrate into focused zones as it percolates into deeper, more reducing environments.

(3) Lastly, as fluids percolate deeper into the aquifer, they carry less dissolved sulfur (mostly as HS^-). The decreasing aH_2S and increasing aH_2 promotes formation of awaruite, as observed in several serpentinites (Klein and Bach, 2009; Schwarzenbach et al., 2021; Steinthorsdottir et al., 2022). Microscopic awaruite is observed in core from Hole BA1B (Fig. 15 in Kelemen et al., 2021), and nanoscale awaruite has been observed in core from Hole BA3A (Ellison et al., 2021), indicating that the highly reducing conditions predicted in our simulations were attained during serpentinite formation. Predicted rock products have ΣS content <0.05 wt% (Fig. 10c, green background). Fluids in equilibrium with these assemblages are alkaline (pH >11, Fig. 10a) and reducing, with $fO_2 < 10^{-80}$ bar (Fig. 10d) and $aH_2 > 0.01$ (Figs. 10e, 11).

The first and second steps outlined above resemble supergene enrichment processes. In supergene enrichment zones lying above porphyry copper deposits, sulfide minerals (e.g., Cu-sulfides) are oxidized at shallow conditions and, as a result, sulfur as sulfate and metals are leached from the protolith during oxidative weathering. These sulfate-bearing solutes are then transported deeper into the aquifer where sulfur and metals reprecipitate at more reducing conditions (Sillitoe, 2005).

Without accumulation of S, for example where groundwater percolates deeper into the aquifer without extensive leaching of S from shallow serpentinites, fluids will evolve with lower aH_2S than that depicted in the reaction path shown in Fig. 11. At these lower aH_2S conditions, formation of magnetite is favored over Fe-sulfides. Nickel, on the other hand, is favored to be precipitated into heazlewoodite, and into awaruite at higher H_2 conditions, rather than pentlandite. In a related setting to Oman, leaching of Ni via oxidative weathering of serpentine soils and bedrock can lead to supergene enrichment of Ni in a saprolitic (serpentine) layer below the limonite (oxide) horizon (Gleeson et al., 2003; Golightly, 1981). In Oman, low-grade Ni laterites have been observed,~3 km east of the MBO sites (Al-Khirbash, 2015, 2020). However, there is no observed enrichment of Ni (and Co, Cu, Zn) corresponding to the presence of sulfur-enriched zones in cores from Holes BA1B and BA4A (see Fig. 1). Overall, in these OmanDP sites, the supergene enrichment is limited to sulfur. We offer an explanation for this in the latter part of the discussion section.

Model results shown in Fig. 10 are from simulations using a representative Oman serpentinized dunite as the reacting protolith. Similar results of models with a representative Oman serpentinized harzburgite as the reacting lithology are depicted in Fig. S6b and show that supergene S enrichment can occur in a harzburgitic aquifer. However, recovered cores primarily identified as harzburgite by the OmanDP lack sulfur-rich zones (Fig. 1). Model results show that a more S-rich zone can occur when dunite is the reacting rock. However, the difference between the two simulations is small (0.45 vs 0.38 wt% ΣS). Reaction kinetics may play a role in this key difference. The dunite reactant yields more brucite at rock-dominated, low water:rock ratios (left side of Fig. 9b) relative to a harzburgite reactant (left side of Fig. S6b). Brucite is a highly reactive mineral (Ellison et al., 2021; Harrison et al., 2015; Kelemen et al., 2011; National Academies of Sciences, Engineering, and Medicine, 2019; Tosca et al., 2018). The decrease in the brucite content of the altered by-products at higher water:rock ratio conditions (solid green curve in Fig. 9b) underscores its reactivity. In models shown in this work and previous experimental and natural serpentinite studies (Ellison et al., 2021; Tutolo et al., 2018), the loss of brucite is mainly via silicification and/or oxidation to serpentine. In addition to silicification, our modeling predicts that some brucite is sulfidized. The precipitation of a mixed sulfide-hydroxide phase resembling those from the tochilinite-valleriite group in a large brucite crystal has been experimentally observed (McCollom et al., 2024). This is consistent with our model results predicting reaction of ferrous-iron-bearing brucite with reduced, sulfur-rich fluids to produce a Mg-rich brucite + pyrrhotite assemblage (i.e., tochilinite) at increasing water:rock ratios (towards the right side of Fig. 9b). This paragenesis, depicted from left to right in Fig. 9b, forms increasingly Mg-rich brucite and higher S contents in the solid product as a given mass of serpentinized dunite reacts with more fluid (i.e., increasing water:rock ratios).

In addition to reaction kinetics, the lack of sulfur-rich zones in the harzburgite layers can be attributed to a lower extent of water-rock interaction (i.e., lower water:rock ratios). The upper portions of Hole BA1B may be close to where sulfur-bearing fluids from the surface are infiltrating, corresponding to a setting characterized by high water:rock ratios (right side of Fig. 9b). In contrast, Hole BA3A might be further along the subsurface fluid path (i.e, low water:rock ratios, left side of Fig. S6a). At low water:rock ratios, the serpentinized harzburgite is relatively S-poor (~0.03 wt% S), where S is mostly precipitated in pyrrhotite. While present, sulfide minerals are less likely to be observable in serpentinites formed at low water:rock conditions (~0.03 wt% S) than those formed at higher water:rock conditions (i.e., >0.4 wt% S, right side of Figs. 9b and S6b). In addition, differences in porosity may influence the local water:rock ratio. In OmanDP cores, serpentinized harzburgites are observed to be less porous than serpentinized dunites (Katayama et al., 2020). Brucite, which is more abundant in serpentinized dunites, can provide porous nanostructures either as dissolution channels or at the interface with olivine and/or serpentine (Chogani and Plümper, 2023; Pujatti et al., 2023). More porous lithologies (e.g., serpentinized dunite) will shift resulting reaction path conditions towards the right side of Fig. 9b, yielding more S-rich by-products.

5.2. What can we learn from the mobilization of critical elements such as Ni from Hole BA1B?

Ultramafic rocks and their alteration products are a major source for critical materials such as Ni (Butt and Cluzel, 2013; Freyssinet et al., 2005; Gleeson et al., 2003; Marsh et al., 2013). The results of mass-transfer reaction-path simulations shown in Figs. 8 and 9 (for dunite reactant) and Figs. S5 and S6 (for harzburgite reactant) provide insights on the fate of nickel during peridotite alteration at low temperature. The dissolved Ni concentration in the evolving fluid remains very low, indicating that it is less mobile than other elements such as S. Instead, Ni is redistributed from the reacting protolith to various secondary minerals in situ. At highly reducing conditions characterized by rock dominated conditions (very low water:rock ratios, left side of Figs. 9b and S6b), nickel is primarily hosted in awaruite. In our simulations, Ni-serpentine and Ni-hydroxide thermodynamic data were included in the serpentine and brucite solid solutions, respectively. However, predicted nickel content of serpentine and brucite is minimal (<0.01 wt% Ni). The Ni concentrations measured in serpentine and brucite mixtures in partially serpentinized harzburgites from Hole BA1B range from 0.02 to 0.8 wt% Ni. We assume a simple ideal site solid solution mixing model in our models. Improvement in solid solution models and refinement of thermodynamic data of serpentine and brucite solid solution component end-members might improve model predictions. Incorporating Ni into a tochilinite solid solution (i.e., haapalaite end-member) could also refine model results. It is possible that Ni measured in the samples are in nano-tochilinite rather than in serpentine and brucite. Moreover, suppressing formation of awaruite in the models, which may be kinetically inhibited at ambient conditions, might increase the predicted Ni concentration in precipitating serpentine and brucite-solid solutions to levels similar to those measured from the Samail ophiolite samples. Additionally, while our models simulate incorporation of Ni into serpentine, brucite, and oxyhydroxides, we did not account for sorption onto mineral surfaces. Ni and other metals can be adsorbed onto the surfaces of hydroxides (e.g., brucite) and oxyhydroxides (e.g., goethite, e.g., Bruemmer et al., 1988). Accounting for both structurally bound and sorbed/exchangeable Ni can refine future modeling efforts.

At intermediate water:rock ratios, such as when the fluid transitions from oxic to reduced, much of the nickel is predicted to be hosted in sulfide minerals (pentlandite and millerite). In oxic conditions, Ni remains mostly in serpentine solid solutions. It is only at very high water:rock ratios that our simulations predict Ni enrichment (Fig. 8) in solid products. At these oxic conditions, much of the protolith has dissolved away, while Ni remains in Fe-rich alteration products composed mostly of goethite and ferric iron rich serpentine. The Ni content of such rocks can be up to 1.2 wt%, similar to that in limonite horizons in nickel laterite deposits. At very high water:rock ratios, some of the Ni is mobilized into the fluid phase. This fluid can then percolate into the saprolite and regolith serpentinite layers of a laterite profile, where it can form supergene Ni saprolitic ores (Freyssinet et al., 2005; Gleeson et al., 2003; Golightly, 1981).

5.3. Microbes can help enrich the rocks in sulfur

Results of microbial community analysis show that sulfate reducing bacteria are likely present in both groundwater and spring water in the Samail ophiolite (Howells et al., 2022; Nothaft et al., 2021a; Rempfert et al., 2017). Metagenomic sequences of subsurface samples collected from the ophiolite (Fones et al., 2019; Kraus et al., 2020) support the presence of sulfate reducers (Templeton et al., 2021). Additionally, radiotracer experiments provide evidence that microbial sulfate reduction is active in Samail ophiolite-hosted aquifers (Glombitza et al.,

2021). Thus, microbial sulfate reducers may have played a role in forming the sulfidic serpentinite zone observed in Holes BA1B and BA4A. However, the extent to which microbes contribute to its formation, relative to *abiotic* sulfide precipitation, is unknown. In supergene copper deposits, while microbial sulfate reducers are known to be present, sulfide precipitation in the metal enriched zone is mostly due to abiotic, inorganic processes (Enders et al., 2006).

Geochemical energy that can be exploited by sulfate reducers is available in fluids hosted in the Samail ophiolite (Canovas et al., 2017; Howells et al., 2022), especially in mixing zones where the presence of both oxidants and reductants yields far-from-equilibrium conditions. Downhole logging data for Hole BA1B and other OmanDP MBO boreholes indicate the presence of reduced, hyperalkaline Type II fluids beneath oxic, slightly alkaline Type I fluids (Kelemen et al., 2021; Templeton et al., 2021). Thus, opportunities for mixing between these two different fluids abound.

In this work, we quantify energy available for various microbial processes that yield sulfides (either dissolved or precipitated as minerals). We simulate consequences of sequentially titrating a calculated Type I end-member fluid (fluid produced at the end of the first step of the dunite-groundwater simulation, black/red star symbol in Fig. 8a) into a model Type II fluid (fluid produced at a water:rock ratio of 1 during the second step of the dunite-groundwater simulation). Results are shown in Fig. 12. A value of 0.5 in the y-axis of Fig. 12 indicates titration (or mixing) of an equal mass of Type I into Type II fluid. Energy is available for hydrogenotrophic sulfate reducers (black curve), following the reaction

$$SO_4^{-2} + H^+ + 4H_2 \rightarrow HS^- + 4H_2O. \quad (1)$$

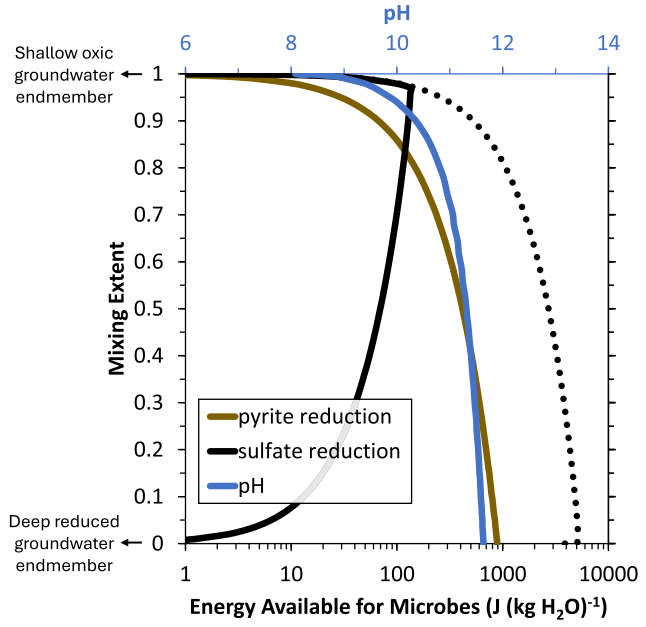

Fig. 12. Predicted energy available for microbial sulfur reducers during mixing of oxic and reduced endmember fluids. The mixing extent indicates the mass proportion of the shallow, oxic groundwater endmember that has been titrated or mixed into deep, reduced groundwater. The black solid curve illustrates the energy available for hydrogenotrophic sulfate reducers (Reaction (1)). The inflection in the slope indicates a change in the limiting reactant from dissolved sulfate at the bottom of the diagram to dissolved hydrogen at the top. The dotted black curve depicts energy available for hydrogenotrophic sulfate reducers assuming no reactant limitations. The brown curve depicts energy available via pyrite reduction (Reaction (3)). (For interpretation of the references to colour in this figure legend, the reader is referred to the web version of this article.)

Available energy increases as more Type I fluid is mixed into Type II fluid, caused by increased availability of the limiting reactant dissolved SO_4^{-2}. At high extents of addition of Type I fluid to Type II fluid, dissolved H_2 becomes the limiting reactant, yielding decreasing amounts of energy provided by Reaction (1). If dissolved sulfate is readily available, and the amount of H_2 is limiting, Reaction (1) can provide much more energy in deeper, Type II dominated mixed fluids (dotted black curve in Fig. 12). Dissolved sulfide (mainly as HS^-) evolved via Reaction (1) can react with dissolved Fe to form FeS or pyrrhotite. Alternatively, dissolved sulfide can react with ferrous iron in brucite to form FeS,

$$Fe(OH)_{2brucite} + HS^- + H^+ \rightarrow FeS + 2H_2O. \quad (2)$$

As dissolved sulfide is precipitated into pyrrhotite (or tochilinite if mixed with brucite), it can promote sulfidation of the host rock. Reaction 2 is likely to be more common in serpentinized dunite relative to serpentinized harzburgite, since dunite contains more brucite.

The reduction of pyrite (FeS_2) precipitated in our reaction path models by H_2 into FeS (or tochilinite) and HS^-,

$$FeS_2 + H_2 \rightarrow FeS + 2HS^- \quad (3)$$

is a viable process that can provide an energy source for microbes and mobilize sulfur from an otherwise insoluble mineral (Spietz et al., 2022). This reaction can provide up to 1000 J per kg mixed fluid (brown curve, Fig. 12), and thus can be a favorable source of energy in mixed ultramafic aquifers.

Overall, there are several opportunities for sulfate and pyrite reducing microbes to exploit energy available in the ultramafic subsurface, especially in scenarios where fluids with contrasting redox states can mix. Up to 100 and 1000 J per kg fluid can be available for sulfate and pyrite reduction, respectively. Assuming 1 vol% or 0.3 wt% porosity, a kg of serpentinized peridotite can supply 0.3 to 3 J of chemotrophic energy. If supply of reactants (dissolved sulfate and H_2) is sustained, a kg of rock in the sulfur enrichment zone can support hundreds of thousands of cells, assuming annual maintenance energy requirement of ~3 μJoules for one sulfate reducing cell (LaRowe and Amend, 2015). Further isotopic work may shed light into the role of microbes in generating this distinct alteration horizon.

6. Conclusions

Three distinct alteration zones were observed in drill core from OmanDP Hole BA1B. A sulfidic serpentinite layer, containing up to 0.6 wt% S is sandwiched between oxidized serpentinite (0–30 m) and serpentinized peridotite (150–400 m). Previous studies have shown that the sulfidic serpentinite zone is mostly composed of serpentine minerals with minor amounts of sulfide, likely of the tochilinite group of minerals (Ellison et al., 2021; Kelemen et al., 2021; Tutolo and Evans, 2018). Further analyses of rocks recovered by the drilling operation and from other sites in Oman, presented here, support previous findings of tochilinite. The presence of this mineral, although minor, results in distinct optically black thin sections that characterize the sulfidic zone. Micro- and nanoanalytical analysis shows that sulfides are hosted in mesh textures after olivine, where serpentine, brucite, and tochilinite co-exist in a mixed assemblage at a nanoscale.

Shipboard analyses of core from Hole BA1B show that while the sulfidic serpentinite zone has elevated S contents relative to the shallow oxidized serpentinite and deeper, partially-serpentinized peridotites, the sulfidic zone is not enriched in elements typically associated with sulfide minerals such as Ni, Co, Cu, and Zn. Shipboard analyses show nearly uniform downhole concentrations for these elements, at concentrations typical of serpentinized peridotites in Oman. Analysis of select samples from Hole BA1B reported here show that Ni is enriched in some mineral alteration products and depleted in others. In the oxidized serpentinite zone, some iron oxyhydroxides contain more than 1 wt% NiO. In the sulfidic serpentinite zone, S-rich mesh textures contain more Ni (Fig. 14

in Kelemen et al., 2021), probably in tochilinite-hapaalite solid solutions. Lastly, in the lower, partially serpentinized zone, Ni is enriched in some mesh textures containing mixtures of serpentine and brucite. It is unclear if Ni in the mesh textures is hosted in serpentine, brucite, nano-sized pentlandtite, or a combination of these minerals. While the listed minerals can contain more Ni than in the bulk compositions or the olivine protolith, other secondary assemblages in the same samples contain far less Ni. Thus, overall, there is no Ni enrichment in either of the three distinct alteration zones in Hole BA1B. We have not discussed distribution of other base metals due to their very low concentrations, which are hard to quantify in our microanalyses. However, our work provides preliminary insights to the fate of Ni during serpentinization, which could be helpful in designing engineered systems that could simultaneously extract critical metals during concurrent carbon mineralization (Kelemen et al., 2024; Wang and Dreisinger, 2022).

Geochemical models simulating the mass transfer between dunite and harzburgite with percolating groundwater explain the formation of the three distinct alteration zones. Oxidized serpentinites are formed during shallow groundwater alteration of serpentinized protoliths, in a system open to atmospheric input. In these oxic conditions, sulfur can be totally dissolved and accumulate in the reacting fluid as dissolved sulfate species. These sulfur-bearing fluids then percolate deeper into the aquifers where atmospheric input is limited. As the fluid becomes more reduced, dissolved sulfur is precipitated in sulfide minerals, accumulating S in the solid products at intermediate depths, akin to the processes that form supergene metal deposits. Following sulfide precipitation, less S-rich fluids percolate deeper into the subsurface aquifer. These fluids ultimately become so reduced that formation of Ni_3Fe alloys (i.e., awaruite) is predicted. These model results support previous findings of these highly reduced minerals in rocks recovered from the MBO sites by the OmanDP (Ellison et al., 2021; Kelemen et al., 2021).

Bioenergetic calculations show that microbial reduction of sulfur into various sulfide-bearing species (dissolved H_2S or HS^-, FeS-bearing minerals such as pyrrhotite or tochilinite) is favorable, supplying up to 1000 J per kg H_2O for sulfur reducing microbes ($\leq \sim 3$ J per kg of rock with 1 vol% porosity). This energy is maximized by mixing of oxic, shallow Type I fluids with reduced, deep Type II fluids, which both occur within the individual MBO boreholes (Fig. 24 in Kelemen et al., 2021). Indeed, evidence for microbial sulfate reduction exists in OmanDP and other nearby wells (Glombitza et al., 2021; Templeton et al., 2021). However, it is unknown to what extent microbial sulfate reducers produce the sulfidic serpentinite horizon, compared to abiotic sulfide precipitation. Isotopic and targeted investigation of samples from Hole BA1B and other nearby wells will provide more insights if sulfide precipitation is predominantly microbial in origin. Likewise, future work could test the involvement of microbial communities in mobilization of sulfur as sulfate in the oxic zones of alteration.

CRediT authorship contribution statement

James Andrew Leong: Writing – review & editing, Writing – original draft, Visualization, Methodology, Investigation, Formal analysis, Data curation, Conceptualization. **Juan Carlos de Obeso:** Writing – review & editing, Methodology, Investigation, Formal analysis, Conceptualization. **Thomas Sharp:** Writing – review & editing, Supervision, Methodology, Formal analysis. **Everett Shock:** Writing – review & editing, Validation, Supervision, Funding acquisition. **Peter Kelemen:** Writing – review & editing, Supervision, Resources, Project administration, Funding acquisition, Conceptualization.

Declaration of competing interest

The authors declare that they have no known competing financial interests or personal relationships that could have appeared to influence the work reported in this paper.

Acknowledgements

We would like to thank Celine Martin and Henrietta Cathey for their assistance in using the EPMA at the AMNH and ASU, respectively. We are also grateful to Jacob Tielke (SEM, LDEO), Kenneth Mossman (FIB, ASU) and John Mardinly (TEM, ASU) for their help in sample analysis. Efforts by Grayson Boyer and the Water Organic Rock Microbe (WORM) portal team enabled thermodynamic simulations conducted in this work. We would also like to thank Damon Teagle, Drew Syverson and the anonymous reviewer for their helpful comments and suggestions. Research for this paper was supported in part by Peter Kelemen's Arthur D. Storke Chair at Columbia University, NSF Research Grant EAR-1516300 (PI: Kelemen), and NSF Research Grant EAR-1515513 (PI: Shock).

This research used samples and/or data provided by the Oman Drilling Program (OmanDP) and would not have been possible without the efforts of the OmanDP and its onsite and shipboard scientific parties. The OmanDP was supported by co-mingled funds from the International Continental Scientific Drilling Project (ICDP; Kelemen, Matter, Teagle Lead PIs), the Alfred P. Sloan Foundation – Deep Carbon Observatory (Grant 2014-3-01, Kelemen PI), the National Science Foundation (NSF-EAR-1516300, Kelemen lead PI), NASA – Astrobiology Institute (NNA15BB02A, Templeton PI), the German Research Foundation (DFG: KO 1723/21-1, Koepke PI), the Japanese Society for the Promotion of Science (JSPS no:16H06347, Michibayashi PI; and KAKENHI 16H02742, Takazawa PI), the European Research Council (Adv: no.669972; Jamveit PI), the Swiss National Science Foundation (SNF:20FI21_163073, Früh-Green PI), JAMSTEC, the TAMU-JR Science Operator, and contributions from the Sultanate of Oman Ministry of Regional Municipalities and Water Resources, the Oman Public Authority of Mining, Sultan Qaboos University, CNRS-Université de Montpellier, Columbia University in the City of New York, and the University of Southampton.

Appendix A. Supplementary data

Supplementary data to this article can be found online at https://doi.org/10.1016/j.lithos.2024.107828.

References

Al-Khirbash, S., 2015. Genesis and mineralogical classification of Ni-laterites, Oman Mountains. Ore Geol. Rev. 65, 199–212. https://doi.org/10.1016/j.oregeorev.2014.09.022.

Al-Khirbash, S.A., 2020. Mineralogical characterization of low-grade nickel laterites from the North Oman Mountains: using mineral liberation analyses – scanning electron microscopy-based automated quantitative mineralogy. Ore Geol. Rev. 120, 103429. https://doi.org/10.1016/j.oregeorev.2020.103429.

Alt, J.C., Schwarzenbach, E.M., Früh-Green, G.L., Shanks, W.C., Bernasconi, S.M., Garrido, C.J., Crispini, L., Gaggero, L., Padrón-Navarta, J.A., Marchesi, C., 2013. The role of serpentinites in cycling of carbon and sulfur: seafloor serpentinization and subduction metamorphism. Lithos 178, 40–54. https://doi.org/10.1016/j.lithos.2012.12.006.

Amend, J.P., LaRowe, D.E., 2019. Minireview: demystifying microbial reaction energetics. Environ. Microbiol. 21, 3539–3547. https://doi.org/10.1111/1462-2920.14778.

Andreani, M., Mével, C., Boullier, A.-M., Escartín, J., 2007. Dynamic control on serpentine crystallization in veins: constraints on hydration processes in oceanic peridotites. Geochem. Geophys. Geosyst. 8. https://doi.org/10.1029/2006GC001373.

Barnes, I., O'Neil, J.R., 1969. The relationship between fluids in some fresh Alpine-type ultramafics and possible modern serpentinization, Western United States. GSA Bull. 80, 1947–1960. https://doi.org/10.1130/0016-7606(1969)80[1947:TRBFIS]2.0.CO;2.

Beard, J.S., Hopkinson, L., 2000. A fossil, serpentinization-related hydrothermal vent, Ocean Drilling Program Leg 173, Site 1068 (Iberia Abyssal Plain): some aspects of mineral and fluid chemistry. J. Geophys. Res. Solid Earth 105, 16527–16539. https://doi.org/10.1029/2000JB900073.

Berner, E.K., Berner, R.A., 2012. Global Environment: Water, air, and geochemical Cycles. Princeton University Press.

Boyer, G., 2021. pyCHNOSZ v0.7.0. https://doi.org/10.5281/ZENODO.5539919.

Boyer, G., Robare, J., Park, N., Ely, T., Shock, E., 2024. AqEquil: Python Package for Aqueous Geochemical Speciation. https://doi.org/10.5281/ZENODO.10476850.

Bradley, J.P., Brownlee, D.E., 1991. An interplanetary dust particle linked directly to type CM meteorites and an asteroidal origin. Science 251, 549–552. https://doi.org/10.1126/science.251.4993.549.

Bruemmer, G.W., Gerth, J., Tiller, K.G., 1988. Reaction kinetics of the adsorption and desorption of nickel, zinc and cadmium by goethite. I. Adsorption and diffusion of metals. J. Soil Sci. 39, 37–52. https://doi.org/10.1111/j.1365-2389.1988.tb01192.x.

Bruni, J., Canepa, M., Chiodini, G., Cioni, R., Cipolli, F., Longinelli, A., Marini, L., Ottonello, G., Vetuschi Zuccolini, M., 2002. Irreversible water–rock mass transfer accompanying the generation of the neutral, Mg–HCO3 and high-pH, Ca–OH spring waters of the Genova province, Italy. Appl. Geochem. 17, 455–474. https://doi.org/10.1016/S0883-2927(01)00113-5.

Butt, C.R.M., Cluzel, D., 2013. Nickel laterite ore deposits: weathered serpentinites. Elements 9, 123–128. https://doi.org/10.2113/gselements.9.2.123.

Canovas, P.A., Hoehler, T., Shock, E.L., 2017. Geochemical bioenergetics during low-temperature serpentinization: an example from the Samail ophiolite, Sultanate of Oman: serpentinization bioenergetics. J. Geophys. Res. Biogeosci. 122, 1821–1847. https://doi.org/10.1002/2017JG003825.

Chavagnac, V., Monnin, C., Ceuleneer, G., Boulart, C., Hoareau, G., 2013. Characterization of hyperalkaline fluids produced by low-temperature serpentinization of mantle peridotites in the Oman and Ligurian ophiolites: hyperalkaline waters in Oman and Liguria. Geochem. Geophys. Geosyst. 14, 2496–2522. https://doi.org/10.1002/ggge.20147.

Chogani, A., Plümper, O., 2023. Decoding the nanoscale porosity in serpentinites from multidimensional electron microscopy and discrete element modelling. Contrib. Mineral. Petrol. 178, 78. https://doi.org/10.1007/s00410-023-02062-4.

de Obeso, J.C., Kelemen, P.B., 2020. Major element mobility during serpentinization, oxidation and weathering of mantle peridotite at low temperatures. Philos. Trans. R. Soc. A Math. Phys. Eng. Sci. 378, 20180433. https://doi.org/10.1098/rsta.2018.0433.

de Obeso, J.C., Santiago Ramos, D.P., Higgins, J.A., Kelemen, P.B., 2020. A Mg isotopic perspective on the mobility of magnesium during serpentinization and carbonation of the Oman ophiolite. J. Geophys. Res. Solid Earth. https://doi.org/10.1029/2020JB020237.

Delacour, A., Früh-Green, G.L., Bernasconi, S.M., Kelley, D.S., 2008. Sulfur in peridotites and gabbros at lost city (30°N, MAR): implications for hydrothermal alteration and microbial activity during serpentinization. Geochim. Cosmochim. Acta 72, 5090–5110. https://doi.org/10.1016/j.gca.2008.07.017.

Dewandel, B., Lachassagne, P., Boudier, F., Al-Hattali, S., Ladouche, B., Pinault, J.-L., Al-Suleimani, Z., 2005. A conceptual hydrogeological model of ophiolite hard-rock aquifers in Oman based on a multiscale and a multidisciplinary approach. Hydrogeol. J. 13, 708–726. https://doi.org/10.1007/s10040-005-0449-2.

Dick, J.M., 2019. CHNOSZ: thermodynamic calculations and diagrams for geochemistry. Front. Earth Sci. 7 (180). https://doi.org/10.3389/feart.2019.00180.

Dódony, I., Buseck, P.R., 2004. Serpentines close-up and intimate: an HRTEM view. Int. Geol. Rev. 46, 507–527. https://doi.org/10.2747/0020-6814.46.6.507.

Ellison, E.T., Templeton, A.S., Zeigler, S.D., Mayhew, L.E., Kelemen, P.B., Matter, J.M., Party, T.O.D.P.S., 2021. Low-temperature hydrogen formation during aqueous alteration of serpentinized peridotite in the Samail ophiolite. J. Geophys. Res. Solid Earth 126. https://doi.org/10.1029/2021JB021981 e2021JB021981.

Ely, T.D., Leong, J.M., Canovas, P.A., Shock, E.L., 2023. Huge variation in H2 generation during seawater alteration of ultramafic rocks. Geochem. Geophys. Geosyst. 24. https://doi.org/10.1029/2022GC010658 e2022GC010658.

Enders, M.S., Knickerbocker, C., Titley, S.R., Southam, G., 2006. The role of bacteria in the supergene environment of the morenci porphyry copper deposit, Greenlee County, Arizona. Econ. Geol. 101, 59–70. https://doi.org/10.2113/gsecongeo.101.1.59.

Evans, B.W., 2004. The serpentinite multisystem revisited: chrysotile is metastable. Int. Geol. Rev. 46, 479–506. https://doi.org/10.2747/0020-6814.46.6.479.

Evans, B.W., Hattori, K., Baronnet, A., 2013. Serpentinite: what, why, where? Elements 9, 99–106. https://doi.org/10.2113/gselements.9.2.99.

Evans, K.A., Frost, B.R., Reddy, S.M., Brown, T.C., 2023. Causes, effects, and implications of the relationships amongst fluids, serpentinisation, and alloys. Lithos 446–447, 107132. https://doi.org/10.1016/j.lithos.2023.107132.

Evans, A.D., Craw, D., Teagle, D.A.H., 2024. Active near-surface mobilisation of slab-derived geochemical signatures by hyperalkaline waters in brecciated serpentinites. Chem. Geol. 643, 121822. https://doi.org/10.1016/j.chemgeo.2023.121822.

Falk, E.S., Kelemen, P.B., 2015. Geochemistry and petrology of listvenite in the Samail ophiolite, Sultanate of Oman: complete carbonation of peridotite during ophiolite emplacement. Geochim. Cosmochim. Acta 160, 70–90. https://doi.org/10.1016/j.gca.2015.03.014.

Fones, E.M., Colman, D.R., Kraus, E.A., Nothaft, D.B., Poudel, S., Rempfert, K.R., Spear, J.R., Templeton, A.S., Boyd, E.S., 2019. Physiological adaptations to serpentinization in the Samail Ophiolite, Oman. ISME J. 13, 1750–1762. https://doi.org/10.1038/s41396-019-0391-2.

Foustoukos, D.I., Bizimis, M., Frisby, C., Shirey, S.B., 2015. Redox controls on Ni–Fe–PGE mineralization and Re/Os fractionation during serpentinization of abyssal peridotite. Geochim. Cosmochim. Acta 150, 11–25. https://doi.org/10.1016/j.gca.2014.11.025.

Freyssinet, P.H., Butt, C.R.M., Morris, R.C., Piantone, P., 2005. Ore-forming processes related to lateritic weathering. In: Hedenquist, J.W., Thompson, J.F.H., Goldfarb, R. J., Richards, J.P. (Eds.), One Hundredth Anniversary Volume. Society of Economic Geologists. https://doi.org/10.5382/AV100.21.

Frost, B.R., 1985. On the stability of sulfides, oxides, and native metals in serpentinite. J. Petrol. 26, 31–63. https://doi.org/10.1093/petrology/26.1.31.

Frost, B.R., Beard, J.S., 2007. On silica activity and serpentinization. J. Petrol. 48, 1351–1368. https://doi.org/10.1093/petrology/egm021.

Frost, B.R., Evans, K.A., Swapp, S.M., Beard, J.S., Mothersole, F.E., 2013. The process of serpentinization in dunite from New Caledonia. Lithos 178, 24–39. https://doi.org/10.1016/j.lithos.2013.02.002.

Gamsjäger, H., Bugajski, J., Gajda, T., Lemire, R.J., Preis, W., 2005. Chemical Thermodynamics of Nickel, Chemical Thermodynamics. Elsevier, Amsterdam; Boston.

Gleeson, S.A., Butt, C.R.M., Elias, M., 2003. Nickel laterites: a review. In: SEG Discovery, pp. 1–18. https://doi.org/10.5382/SEGnews.2003-54.fea.

Glein, C.R., Zolotov, M.Y., 2020. Hydrogen, hydrocarbons, and habitability across the solar system. Elements 16, 47–52. https://doi.org/10.2138/gselements.16.1.47.

Glombitza, C., Putman, L.I., Rempfert, K.R., Kubo, M.D., Schrenk, M.O., Templeton, A.S., Hoehler, T.M., 2021. Active microbial sulfate reduction in fluids of serpentinizing peridotites of the continental subsurface. Commun. Earth Environ. 2, 1–9. https://doi.org/10.1038/s43247-021-00157-z.

Godard, M., Jousselin, D., Bodinier, J.-L., 2000. Relationships between geochemistry and structure beneath a palaeo-spreading centre: a study of the mantle section in the Oman ophiolite. Earth Planet. Sci. Lett. 180, 133–148. https://doi.org/10.1016/S0012-821X(00)00149-7.

Golightly, J.P., 1981. Nickeliferous Laterite Deposits. https://doi.org/10.5382/AV75.18.

Hanghøj, K., Kelemen, P.B., Hassler, D., Godard, M., 2010. Composition and genesis of depleted mantle peridotites from the Wadi Tayin Massif, Oman Ophiolite; major and trace element geochemistry, and Os isotope and PGE systematics. J. Petrol. 51, 201–227. https://doi.org/10.1093/petrology/egp077.

Harrison, A.L., Dipple, G.M., Power, I.M., Mayer, K.U., 2015. Influence of surface passivation and water content on mineral reactions in unsaturated porous media: implications for brucite carbonation and CO2 sequestration. Geochim. Cosmochim. Acta 148, 477–495. https://doi.org/10.1016/j.gca.2014.10.020.

Hatakeyama, K., Katayama, I., Abe, N., Okazaki, K., Michibayashi, K., Party, the O.D.P.S, 2021. Effects of alteration and cracks on the seismic velocity structure of oceanic lithosphere inferred from ultrasonic measurements of mafic and ultramafic samples collected by the Oman Drilling Project. J. Geophys. Res. Solid Earth 126. https://doi.org/10.1029/2021JB021923 e2021JB021923.

Helgeson, H.C., Delaney, J.M., Nesbitt, H.W., Bird, D.K., 1978. Summary and critique of the thermodynamic properties of rock-forming minerals. Am. J. Sci. 278, 1–229.

Hong, G., Till, J.L., Greve, A., Lee, S.-M., Party, the O.D.P.P. 2 S, 2022. New rock magnetic analysis of ultramafic cores from the Oman Drilling Project and its implications for alteration of lower crust and upper mantle. J. Geophys. Res. Solid Earth 127. https://doi.org/10.1029/2022JB024379 e2022JB024379.

Howells, A.E.G., Leong, J.A.M., Ely, T., Santana, M., Robinson, K., Esquivel-Elizondo, S., Cox, A., Poret-Peterson, A., Krajmalnik-Brown, R., Shock, E.L., 2022. Energetically informed niche models of hydrogenotrophs detected in sediments of serpentinized fluids of the Samail ophiolite of Oman. J. Geophys. Res. Biogeosci. 127. https://doi.org/10.1029/2021JG006317.

Katayama, I., Abe, N., Hatakeyama, K., Akamatsu, Y., Okazaki, K., Ulven, O.I., Hong, G., Zhu, W., Cordonnier, B., Michibayashi, K., Godard, M., Kelemen, P., Party, the O.D.P.P. 2 S, 2020. Permeability profiles across the crust-mantle sections in the Oman Drilling Project inferred from dry and wet resistivity data. J. Geophys. Res. Solid Earth 125. https://doi.org/10.1029/2019JB018698 e2019JB018698.

Kelemen, P.B., Matter, J., Streit, E.E., Rudge, J.F., Curry, W.B., Blusztajn, J., 2011. Rates and mechanisms of mineral carbonation in peridotite: natural processes and recipes for enhanced, in situ CO2 capture and storage. Annu. Rev. Earth Planet. Sci. 39, 545–576. https://doi.org/10.1146/annurev-earth-092010-152509.

Kelemen, P.B., Matter, J.M., Teagle, D.A.H., Coggon, J.A., 2020a. Proceedings of the Oman Drilling Project: Scientific Drilling in the Samail Ophiolite, Sultanate of Oman, Proceedings of the International Ocean Discovery Program. International Ocean Discovery Program. https://doi.org/10.14379/OmanDP.proc.2020.

Kelemen, P.B., Matter, J.M., Teagle, D.A.H., Coggon, J.A., Oman Drilling Project Science Team, 2020b. Site BA1. In: Proceedings of the Oman Drilling Project: Scientific Drilling in the Samail Ophiolite, Sultanate of Oman, Proceedings of the International Ocean Discovery Program. International Ocean Discovery Program. https://doi.org/10.14379/OmanDP.proc.2020.

Kelemen, P.B., Matter, J.M., Teagle, D.A.H., Coggon, J.A., Oman Drilling Project Science Team, 2020c. Site BA2. In: Proceedings of the Oman Drilling Project: Scientific Drilling in the Samail Ophiolite, Sultanate of Oman, Proceedings of the International Ocean Discovery Program. International Ocean Discovery Program. https://doi.org/10.14379/OmanDP.proc.2020.

Kelemen, P.B., Matter, J.M., Teagle, D.A.H., Coggon, J.A., Oman Drilling Project Science Team, 2020d. Site BA3. In: Proceedings of the Oman Drilling Project: Scientific Drilling in the Samail Ophiolite, Sultanate of Oman, Proceedings of the International Ocean Discovery Program. International Ocean Discovery Program. https://doi.org/10.14379/OmanDP.proc.2020.

Kelemen, P.B., Matter, J.M., Teagle, D.A.H., Coggon, J.A., Oman Drilling Project Science Team, 2020e. Site BA4. In: Proceedings of the Oman Drilling Project: Scientific Drilling in the Samail Ophiolite, Sultanate of Oman, Proceedings of the International Ocean Discovery Program. International Ocean Discovery Program. https://doi.org/10.14379/OmanDP.proc.2020.

Kelemen, P.B., Matter, J.M., Teagle, D.A.H., Coggon, J.A., Oman Drilling Project Science Team, 2020f. Methods and explanatory notes. In: Proceedings of the Oman Drilling Project: Scientific Drilling in the Samail Ophiolite, Sultanate of Oman, Proceedings of the International Ocean Discovery Program. International Ocean Discovery Program. https://doi.org/10.14379/OmanDP.proc.2020.

Kelemen, P.B., Leong, J.A., Carlos de Obeso, J., Matter, J.M., Ellison, E.T., Templeton, A., Nothaft, D.B., Eslami, A., Evans, K., Godard, M., Malvoisin, B., Coggon, J.A., Warsi, N.H., Pézard, P., Choe, S., Teagle, D.A.H., Michibayashi, K., Takazawa, E., Al

Sulaimani, Z., Team, T.O.D.P.S, 2021. Initial results from the Oman Drilling Project multi-borehole observatory: petrogenesis and ongoing alteration of mantle peridotite in the weathering horizon. J. Geophys. Res. Solid Earth 126. https://doi.org/10.1029/2021JB022729 e2021JB022729.

Kelemen, P.B., Leong, J.M., Schaef, T., Nagurney, A., 2024. Combining CO2 storage via carbon mineralization with Ni & Co extraction from peridotite and serpentinite mine tailings. In: Presented at the AGU Fall Meeting, Washington, D. C.

Khedr, M.Z., Arai, S., Python, M., Tamura, A., 2014. Chemical variations of abyssal peridotites in the central Oman ophiolite: evidence of oceanic mantle heterogeneity. Gondwana Res. 25, 1242–1262. https://doi.org/10.1016/j.gr.2013.05.010.

Klein, F., Bach, W., 2009. Fe–Ni–Co–O–S phase relations in peridotite–seawater interactions. J. Petrol. 50, 37–59. https://doi.org/10.1093/petrology/egn071.

Kraus, E.A., Nothaft, D., Stamps, B.W., Rempfert, K.R., Ellison, E.T., Matter, J.M., Templeton, A.S., Boyd, E.S., Spear, J.R., 2020. Molecular evidence for an active microbial methane cycle in subsurface serpentinite-hosted groundwaters in the Samail ophiolite, Oman. Appl. Environ. Microbiol. https://doi.org/10.1128/AEM.02068-20.

Lang, S.Q., Butterfield, D.A., Schulte, M., Kelley, D.S., Lilley, M.D., 2010. Elevated concentrations of formate, acetate and dissolved organic carbon found at the lost city hydrothermal field. Geochim. Cosmochim. Acta 74, 941–952. https://doi.org/10.1016/j.gca.2009.10.045.

LaRowe, D.E., Amend, J.P., 2015. Catabolic rates, population sizes and doubling/replacement times of microorganisms in natural settings. Am. J. Sci. 315, 167–203. https://doi.org/10.2475/03.2015.01.

Leong, J.A.M., Shock, E.L., 2020. Thermodynamic constraints on the geochemistry of low-temperature, continental, serpentinization-generated fluids. Am. J. Sci. 320, 185–235. https://doi.org/10.2475/03.2020.01.

Leong, J.A.M., Howells, A.E., Robinson, K.J., Cox, A., Debes, R.V., Fecteau, K., Prapaipong, P., Shock, E.L., 2021. Theoretical predictions versus environmental observations on serpentinization fluids: lessons from the Samail ophiolite in Oman. J. Geophys. Res. Solid Earth 126. https://doi.org/10.1029/2020JB020756 e2020JB020756.

Lima-Zaloumis, J., Neubeck, A., Ivarsson, M., Bose, M., Greenberger, R., Templeton, A.S., Czaja, A.D., Kelemen, P.B., Edvinsson, T., 2022. Microbial biosignature preservation in carbonated serpentine from the Samail Ophiolite, Oman. Commun. Earth Environ. 3, 1–11. https://doi.org/10.1038/s43247-022-00551-1.

Lods, G., Roubinet, D., Matter, J.M., Leprovost, R., Gouze, P., 2020. Groundwater flow characterization of an ophiolitic hard-rock aquifer from cross-borehole multi-level hydraulic experiments. J. Hydrol. 589, 125152. https://doi.org/10.1016/j.jhydrol.2020.125152.

Mackinnon, I.D.R., Zolensky, M.E., 1984. Proposed structures for poorly characterized phases in C2M carbonaceous chondrite meteorites. Nature 309, 240–242. https://doi.org/10.1038/309240a0.

Malvoisin, B., Zhang, C., Müntener, O., Baumgartner, L.P., Kelemen, P.B., Party, O.D.P.S., 2020. Measurement of volume change and mass transfer during serpentinization: insights from the Oman Drilling Project. J. Geophys. Res. Solid Earth 125. https://doi.org/10.1029/2019JB018877 e2019JB018877.

Marsh, E.E., Anderson, E.D., Gray, F., 2013. Nickel-cobalt laterites: a deposit model (No. 2010-5070- H). In: Scientific Investigations Report. U.S. Geological Survey. https://doi.org/10.3133/sir20105070H.

Matter, J.M., Waber, H.N., Loew, S., Matter, A., 2006. Recharge areas and geochemical evolution of groundwater in an alluvial aquifer system in the Sultanate of Oman. Hydrogeol. J. 14, 203–224. https://doi.org/10.1007/s10040-004-0425-2.

Mayhew, L.E., Ellison, E.T., 2020. A synthesis and meta-analysis of the Fe chemistry of serpentinites and serpentine minerals. Philos. Trans. R. Soc. A Math. Phys. Eng. Sci. 378, 20180420. https://doi.org/10.1098/rsta.2018.0420.

McCollom, T.M., Hoehler, T., Fike, D.A., Houghton, J.L., Bell, A., Klein, F., Moskowitz, B., Solheid, P., 2024. Formation of mixed-layer sulfide-hydroxide minerals from the Tochilinite-Valleriite group during experimental serpentinization of olivine. Am. Mineral. 109, 61–72. https://doi.org/10.2138/am-2022-8625.

Miller, H.M., Matter, J.M., Kelemen, P., Ellison, E.T., Conrad, M.E., Fierer, N., Ruchala, T., Tominaga, M., Templeton, A.S., 2016. Modern water/rock reactions in Oman hyperalkaline peridotite aquifers and implications for microbial habitability. Geochim. Cosmochim. Acta 179, 217–241. https://doi.org/10.1016/j.gca.2016.01.033.

Monnier, C., Girardeau, J., Le Mée, L., Polvé, M., 2006. Along-ridge petrological segmentation of the mantle in the Oman ophiolite. Geochem. Geophys. Geosyst. 7. https://doi.org/10.1029/2006GC001320.

National Academies of Sciences, Engineering, and Medicine, 2019. Chapter 6: carbon mineralization of CO2. In: Negative Emissions Technologies and Reliable Sequestration: A Research Agenda. National Academies Press, Washington, D.C, pp. 247–318. https://doi.org/10.17226/25259.

Neal, C., Shand, P., 2002. Spring and surface water quality of the Cyprus ophiolites. Hydrol. Earth Syst. Sci. 6, 797–817. https://doi.org/10.5194/hess-6-797-2002.

Neal, C., Stanger, G., 1985. Past and present serpentinisation of ultramafic rocks; an example from the Semail Ophiolite Nappe of Northern Oman. In: The Chemistry of Weathering. Springer, pp. 249–275.

Negishi, H., Arai, S., Yurimoto, H., Ito, S., Ishimaru, S., Tamura, A., Akizawa, N., 2013. Sulfide-rich dunite within a thick Moho transition zone of the northern Oman ophiolite: implications for the origin of Cyprus-type sulfide deposits. Lithos 164–167, 22–35. https://doi.org/10.1016/j.lithos.2012.11.024.

Neveu, M., Desch, S.J., Castillo-Rogez, J.C., 2017. Aqueous geochemistry in icy world interiors: equilibrium fluid, rock, and gas compositions, and fate of antifreezes and radionuclides. Geochim. Cosmochim. Acta 212, 324–371. https://doi.org/10.1016/j.gca.2017.06.023.

Nicolas, A., Boudier, F., Ildefonse, B., Ball, E., 2000. Accretion of Oman and United Arab Emirates ophiolite – discussion of a new structural map. Mar. Geophys. Res. 21, 147–180. https://doi.org/10.1023/A:1026769727917.

Nothaft, D.B., Templeton, A.S., Boyd, E.S., Matter, J.M., Stute, M., Paukert Vankeuren, A. N., Team, T.O.D.P.S, 2021a. Aqueous geochemical and microbial variation across discrete depth intervals in a peridotite aquifer assessed using a packer system in the Samail ophiolite, Oman. J. Geophys. Res. Biogeosci. 126. https://doi.org/10.1029/2021JG006319 e2021JG006319.

Nothaft, D.B., Templeton, A.S., Rhim, J.H., Wang, D.T., Labidi, J., Miller, H.M., Boyd, E. S., Matter, J.M., Ono, S., Young, E.D., Kopf, S.H., Kelemen, P.B., Conrad, M.E., Team, T.O.D.P.S., 2021b. Geochemical, biological, and clumped isotopologue evidence for substantial microbial methane production under carbon limitation in serpentinites of the Samail ophiolite, Oman. J. Geophys. Res. Biogeosci. 126. https://doi.org/10.1029/2020JG006025 e2020JG006025.

Oeser, M., Strauss, H., Wolff, P.E., Koepke, J., Peters, M., Garbe-Schönberg, D., Dietrich, M., 2012. A profile of multiple sulfur isotopes through the Oman ophiolite. Chem. Geol. 312–313, 27–46. https://doi.org/10.1016/j.chemgeo.2012.04.008.

O'Hanley, D.S., 1992. Solution to the volume problem in serpentinization. Geology 20, 705–708. https://doi.org/10.1130/0091-7613(1992)020<0705:STTVPI>2.3.CO;2.

Organova, N.I., Gorshkov, A.I., Dikov, Y.P., Kul'bachinskiy, V.A., Laputina, I.P., Sivtsov, A.V., Sluzhenikin, S.F., Ponomarenko, A.I., 1988. New data on Tochilinite. Int. Geol. Rev. https://doi.org/10.1080/00206818809466050.

Paukert Vankeuren, A.N., Matter, J.M., Stute, M., Kelemen, P.B., 2019. Multitracer determination of apparent groundwater ages in peridotite aquifers within the Samail ophiolite, Sultanate of Oman. Earth Planet. Sci. Lett. 516, 37–48. https://doi.org/10.1016/j.epsl.2019.03.007.

Paukert, A.N., Matter, J.M., Kelemen, P.B., Shock, E.L., Havig, J.R., 2012. Reaction path modeling of enhanced in situ CO2 mineralization for carbon sequestration in the peridotite of the Samail Ophiolite, Sultanate of Oman. Chem. Geol. 330–331, 86–100. https://doi.org/10.1016/j.chemgeo.2012.08.013.

Pujatti, S., Plümper, O., Tutolo, B.M., 2023. Weathering-driven porosity generation in altered oceanic peridotites. Earth Planet. Sci. Lett. 604, 118006. https://doi.org/10.1016/j.epsl.2023.118006.

Rempfert, K.R., Miller, H.M., Bompard, N., Nothaft, D., Matter, J.M., Kelemen, P., Fierer, N., Templeton, A.S., 2017. Geological and geochemical controls on subsurface microbial life in the Samail Ophiolite, Oman. Front. Microbiol. 8 (56). https://doi.org/10.3389/fmicb.2017.00056.

Rempfert, K.R., Nothaft, D.B., Kraus, E.A., Asamoto, C.K., Evans, R.D., Spear, J.R., Matter, J.M., Kopf, S.H., Templeton, A.S., 2023. Subsurface biogeochemical cycling of nitrogen in the actively serpentinizing Samail Ophiolite, Oman. Front. Microbiol. 14. https://doi.org/10.3389/fmicb.2023.1139633.

Schrenk, M.O., Brazelton, W.J., Lang, S.Q., 2013. Serpentinization, carbon, and deep life. Rev. Mineral. Geochem. 75, 575–606. https://doi.org/10.2138/rmg.2013.75.18.

Schwarzenbach, E.M., Früh-Green, G.L., Bernasconi, S.M., Alt, J.C., Shanks III, W.C., Gaggero, L., Crispini, L., 2012. Sulfur geochemistry of peridotite-hosted hydrothermal systems: comparing the Ligurian ophiolites with oceanic serpentinites. Geochim. Cosmochim. Acta 91, 283–305. https://doi.org/10.1016/j.gca.2012.05.021.

Schwarzenbach, E.M., Gazel, E., Caddick, M.J., 2014. Hydrothermal processes in partially serpentinized peridotites from Costa Rica: evidence from native copper and complex sulfide assemblages. Contrib. Mineral. Petrol. 168, 1079. https://doi.org/10.1007/s00410-014-1079-2.

Schwarzenbach, E.M., Vrijmoed, J.C., Engelmann, J.M., Liesegang, M., Wiechert, U., Rohne, R., Plümper, O., 2021. Sulfide dissolution and awaruite formation in continental serpentinization environments and its implications to supporting life. J. Geophys. Res. Solid Earth 126. https://doi.org/10.1029/2021JB021758 e2021JB021758.

Scicchitano, M.R., Spicuzza, M.J., Ellison, E.T., Tuschel, D., Templeton, A.S., Valley, J. W., 2021. In situ oxygen isotope determination in serpentine minerals by SIMS: addressing matrix effects and providing new insights on serpentinisation at hole BA1B (Samail ophiolite, Oman). Geostand. Geoanal. Res. 45, 161–187. https://doi.org/10.1111/ggr.12359.

Shock, E., Canovas, P., 2010. The potential for abiotic organic synthesis and biosynthesis at seafloor hydrothermal systems. Geofluids 10, 161–192. https://doi.org/10.1111/j.1468-8123.2010.00277.x.

Shock, E.L., Helgeson, H.C., 1988. Calculation of the thermodynamic and transport properties of aqueous species at high pressures and temperatures: correlation algorithms for ionic species and equation of state predictions to 5 kb and 1000°C. Geochim. Cosmochim. Acta 52, 2009–2036. https://doi.org/10.1016/0016-7037(88)90181-0.

Shock, E.L., Oelkers, E.H., Johnson, J.W., Sverjensky, D.A., Helgeson, H.C., 1992. Calculation of the thermodynamic properties of aqueous species at high pressures and temperatures. Effective electrostatic radii, dissociation constants and standard partial molal properties to 1000 C and 5 kbar. J. Chem. Soc. Faraday Trans. 88, 803–826. https://doi.org/10.1039/FT9928800803.

Shock, E.L., Sassani, D.C., Willis, M., Sverjensky, D.A., 1997. Inorganic species in geologic fluids: correlations among standard molal thermodynamic properties of aqueous ions and hydroxide complexes. Geochim. Cosmochim. Acta 61, 907–950. https://doi.org/10.1016/S0016-7037(96)00339-0.

Shock, E.L., Holland, M., Meyer-Dombard, D., Amend, J.P., Osburn, G.R., Fischer, T.P., 2010. Quantifying inorganic sources of geochemical energy in hydrothermal ecosystems, Yellowstone National Park, USA. Geochim. Cosmochim. Acta 74, 4005–4043. https://doi.org/10.1016/j.gca.2009.08.036.

Sillitoe, R.H., 2005. Supergene oxidized and enriched porphyry copper and related deposits. In: Hedenquist, J.W., Thompson, J.F.H., Goldfarb, R.J., Richards, J.P.

(Eds.), One Hundredth Anniversary Volume. Society of Economic Geologists. https://doi.org/10.5382/AV100.22.

Sohn, R.A., Matter, J.M., 2023. The response of borehole water levels in an ophiolitic, peridotite aquifer to atmospheric, solid Earth, and ocean tides. J. Hydrol. X 21, 100163. https://doi.org/10.1016/j.hydroa.2023.100163.

Spietz, R.L., Payne, D., Kulkarni, G., Metcalf, W.W., Roden, E.E., Boyd, E.S., 2022. Investigating abiotic and biotic mechanisms of pyrite reduction. Front. Microbiol. 13. https://doi.org/10.3389/fmicb.2022.878387.

Steinthorsdottir, K., Dipple, G.M., Cutts, J.A., Turvey, C.C., Milidragovic, D., Peacock, S. M., 2022. Formation and preservation of brucite and awaruite in serpentinized and tectonized mantle in Central British Columbia: implications for carbon mineralization and nickel mining. J. Petrol. 63, egac100. https://doi.org/10.1093/petrology/egac100.

Sverjensky, D.A., Shock, E.L., Helgeson, H.C., 1997. Prediction of the thermodynamic properties of aqueous metal complexes to 1000°C and 5 kb. Geochim. Cosmochim. Acta 61, 1359–1412. https://doi.org/10.1016/S0016-7037(97)00009-4.

Templeton, A.S., Ellison, E.T., 2020. Formation and loss of metastable brucite: does Fe (II)-bearing brucite support microbial activity in serpentinizing ecosystems? Philos. Trans. R. Soc. A Math. Phys. Eng. Sci. 378, 20180423. https://doi.org/10.1098/rsta.2018.0423.

Templeton, A.S., Ellison, E.T., Glombitza, C., Morono, Y., Rempfert, K.R., Hoehler, T.M., Zeigler, S.D., Kraus, E.A., Spear, J.R., Nothaft, D.B., Fones, E.M., Boyd, E.S., Munro-Ehrlich, M., Mayhew, L.E., Cardace, D., Matter, J.M., Kelemen, P.B., Party, the O.D. P.S, 2021. Accessing the subsurface biosphere within rocks undergoing active low-temperature serpentinization in the Samail ophiolite (Oman Drilling Project). J. Geophys. Res. Biogeosci. 126. https://doi.org/10.1029/2021JG006315 e2021JG006315.

Templeton, A.S., Ellison, E.T., Kelemen, P.B., Leong, J., Boyd, E.S., Colman, D.R., Matter, J.M., 2024. Low-temperature hydrogen production and consumption in partially-hydrated peridotites in Oman: implications for stimulated geological hydrogen production. Front. Geochem. 2. https://doi.org/10.3389/fgeoc.2024.1366268.

Ternieten, L., Früh-Green, G.L., Bernasconi, S.M., 2021. Carbon geochemistry of the active serpentinization site at the Wadi Tayin Massif: insights from the ICDP Oman Drilling Project: phase II. J. Geophys. Res. Solid Earth 126. https://doi.org/10.1029/2021JB022712 e2021JB022712.

Tosca, N.J., Ahmed, I.A.M., Tutolo, B.M., Ashpitel, A., Hurowitz, J.A., 2018. Magnetite authigenesis and the warming of early Mars. Nat. Geosci. 11, 635–639. https://doi.org/10.1038/s41561-018-0203-8.

Tutolo, B.M., Evans, K.A., 2018. Tochilinite occurrence in serpentinized peridotite from the Samail ophiolite. In: Presented at the AGU 2018. V13E-0160.

Tutolo, B.M., Luhmann, A.J., Tosca, N.J., Seyfried, W.E., 2018. Serpentinization as a reactive transport process: the brucite silicification reaction. Earth Planet. Sci. Lett. 484, 385–395. https://doi.org/10.1016/j.epsl.2017.12.029.

Tutolo, B.M., Seyfried, W.E., Tosca, N.J., 2020. A seawater throttle on H2 production in Precambrian serpentinizing systems. PNAS 117, 14756–14763. https://doi.org/10.1073/pnas.1921042117.

Wang, F., Dreisinger, D., 2022. Carbon mineralization with concurrent critical metal recovery from olivine. Proc. Natl. Acad. Sci. 119. https://doi.org/10.1073/pnas.2203937119 e2203937119.

Wicks, F.J., Whittaker, E.J.W., 1977. Serpentine textures and serpentinization. Can. Mineral. 15, 459–488.

Wolery, T., Jarek, R., 2003. EQ3/6, Version 8.0, Software User's Manual (No. 10813-UM- 8.0– 00). US Department of Energy, Office of Civilian Radioactive Waste Management, Office of Repository Development, Las Vegas, Nevada.